# Detection of Spin Orbit Resonances in advance gravitational wave detector era


A thesis submitted towards partial fulfilment of
BS-MS Dual Degree Programme

by

Chaitanya Afle

under the guidance of

Prof. Sanjit Mitra

Inter-University Centre for Astronomy and
Astrophysics (IUCAA), Pune

Indian Institute of Science Education and Research
Pune

# Certificate

This is to certify that this thesis entitled DETECTION OF SPIN ORBIT RESONANCES IN ADVANCE GRAVITATIONAL WAVE DETECTOR ERA submitted towards the partial fulfillment of the BS-MS dual degree programme at the Indian Institute of Science Education and Research Pune represents original research carried out by CHAITANYA AFLE at INTER-UNIVERSITY CENTRE FOR ASTRONOMY AND ASTROPHYSICS (IUCAA), PUNE, under the supervision of PROF. SANJIT MITRA during the academic year 2015-2016.

Student
CHAITANYA AFLE

Supervisor
PROF. SANJIT MITRA

# Declaration

I hereby declare that the matter embodied in the report entitled Detection of Spin Orbit Resonances in Advance Gravitational Wave Detector Era are the results of the investigations carried out by me at the Inter-University Centre for Astronomy and Astrophysics (IUCAA), Pune, under the supervision of Prof. Sanjit Mitra and the same has not been submitted elsewhere for any other degree.

Student
Chaitanya Afle

Supervisor
Prof. Sanjit
Mitra

# Acknowledgements

This project has been a great learning experience for me and I would like to thank everyone who has helped me make it an enjoyable journey as well.

First of all, I would like to thank Prof. Sanjit Mitra for agreeing to be my project advisor. I am grateful to him for his constant support, motivation and patience. I thank him for dedicating his time to me whenever I needed his help.

A very special thanks goes to my co-advisor Anuradha Gupta for helping me throughout the year. I look up to her work ethics and dedication, and hope to achieve that myself someday. I cannot thank her enough for guiding me in this project and solving my doubts.

I am also deeply grateful to Bhooshan Gadre, from whom I have learned immensely about gravitational waves. I thank him for his support and advice, and for encouraging me to have fun while working.

I would also like to thank Archisman Ghosh, Nairwita Mazumder and Prayush Kumar for their help with the work in this project. I also thank the entire GW group at IUCAA.

I also thank Prof. Prasad Subramanian for agreeing to be my mentor for the project.

I thank all my friends at IISER and outside - Shivani, Akshay, Sharvaree, Kalyanee, Sohan and Harsha, for their support and care has helped me remain focused. I thank them all for these wonderful five years at IISER and for sharing all the fun times. I also thank Bhagyashree maushi and Paresh kaka for their constant support and care.

Lastly, I thank my mother and my father for loving me so dearly. Thank you for always encouraging and motivating me, and standing by me in times good and bad.

# Abstract

Very recently, LIGO Scientific collaboration has made the first direct detection of gravitational waves (GWs) emitted from two coalescing stellar mass black holes (BHs). This detection, with the advanced GW detectors, has given hope to detect more and more coalescing binaries, helping us to reveal their interesting properties. There exist certain equilibrium configurations in spinning and precessing binaries in which spins of the BHs and orbital angular momentum of the binary remain in a plane (the resonant plane) during their evolution. The spin-orbit resonances have important astrophysical implications as the evolution and subsequent coalescence of super-massive BH binaries in this configuration leads to low recoil velocities of merger remnants. Hence, the final BHs will be retained in their host galaxies that are formed from the merger of smaller galaxies. Moreover, it has been shown that the BH spins in comparable mass stellar mass binary would preferentially lie in a resonant plane when their GWs enter the advanced LIGO frequency band. Therefore, it is highly desirable to investigate the detectability of such systems in advanced GW detector era which can, in turn, improve our perception of their high mass counterparts. The current detection pipelines involve only non-spinning and non-precessing template banks for compact binary searches. In this thesis, we test the performance of these template banks in detecting spin-orbit resonant binaries. We find that the full inspiral-merger-ringdown template banks are performing better in detecting resonant binaries as compared to inspiral-only banks. We show that generically precessing binaries can also be detected with statistically equal probability as resonant binaries. We give equilibrium solutions for the sub-maximally spinning BH binaries, which were not studied in detail previously.

# Contents

# Chapter 1

# Gravitational Waves: an overview

Albert Einstein presented his theory of general relativity almost a century back. In it he described how gravity can be thought of as curvature of space-time due to the presence of mass or energy, rather than a physical force. This curvature, in turn, determines how the matter must move. One of the most fascinating implications of the theory was the existence of *gravitational waves*. Gravitational waves (GWs) are often referred to as ripples in the fabric of space-time. The theory suggests that when massive bodies accelerate, gravitational radiation is emitted that carries the energy away.

Gravitational waves were directly detected for the first time last year in September by the LIGO (Laser Interferometric Gravitational wave Observatory) detectors, operated by the LIGO Scientific Collaboration (LSC) [1]. Prior to this detection, we only had an indirect observation of GWs from the Hulse-Taylor binary pulsar [2]. This direct detection of GWs would revolutionize the way we look at astronomy and cosmology. Throughout the history, we have been detecting information from the space in the form of electromagnetic waves. Now, since we are able to detect GWs, it will open new doors of observational science. They offer a unique probe into some of the most intriguing systems of our universe, which is not possible otherwise. Primordial GWs can actually tell us about the very early universe right after the Big Bang.

The physics of GWs is itself very exciting, incorporating various theoretical domains such as general relativity, astrophysics, field theory, etc. and also experimental techniques that aim towards more accurate detection with lesser and lesser noise. As exciting as the field is, it is also very challenging. The ripples in the fabric of space-time are created by enormous masses undergoing rapid accelerations. However, we know that gravity is the weakest of the four fundamental interactions. That is why the strength of the GWs at the detectors on the Earth,

coming from a far away source (for example, a coalescing binary system) is very small. Detecting a strong GW is equivalent of measuring relative displacements of the order of $10^{-18}$ m (see Sec. 1.3), which is less than the size of a proton by a factor of 1000. It is increasingly challenging to detect weaker Gws.

The next section discusses the formalism of GWs, including the derivation of the wave equation from general relativity.

## 1.1 Formalism

Gravitational Waves are the solutions to Einstein's equation in the weak field limit. Einstein's equation governs the relation between space-time curvature and energy - momentum:

$$G_{\alpha\beta} = R_{\alpha\beta} - \frac{1}{2} g_{\alpha\beta} R = \frac{8\pi G}{c^4} T_{\alpha\beta} \ , \tag{1.1}$$

where $g_{\alpha\beta}$ denotes the metric tensor, $R_{\alpha\beta}$ the Ricci curvature tensor, $R$ the Ricci scalar, $T_{\alpha\beta}$ the stress-energy tensor and $G_{\alpha\beta}$ the Einstein tensor. In this section, we derive the wave equations for GW and then discuss about the polarizations of GWs.

### 1.1.1 Derivation of the Gravitational Wave Equation

The wave equation can be derived from the weak field approximation to general relativity, in which space-time is nearly flat and we can use Lorentz coordinates[3, 4]. The metric $g_{\alpha\beta}$ is separated into the flat Minkowski metric $\eta_{\alpha\beta}$ and a perturbation term $h_{\alpha\beta}$:

$$g_{\alpha\beta} = \eta_{\alpha\beta} + h_{\alpha\beta} \ , \tag{1.2}$$

where $|h_{\alpha\beta}| << 1$ and

$$\eta_{\alpha\beta} = \begin{pmatrix} -1 & 0 & 0 & 0 \\ 0 & 1 & 0 & 0 \\ 0 & 0 & 1 & 0 \\ 0 & 0 & 0 & 1 \end{pmatrix} \ . \tag{1.3}$$

We raise (and lower) the indices of the perturbation term with $\eta_{\alpha\beta}$:

$$h^{\alpha\beta} = \eta^{\alpha\gamma} \eta^{\beta\delta} h_{\gamma\delta} \ . \tag{1.4}$$

So the inverse metric (correct to first order) will be:

$$g^{\alpha\beta} = \eta^{\alpha\beta} - h^{\alpha\beta} \ . \tag{1.5}$$

Also, the trace-reversed metric perturbation will be:

$$\overline{h}_{\alpha\beta} = h_{\alpha\beta} - \frac{1}{2}\eta_{\alpha\beta}h \ , \tag{1.6}$$

where $h = \eta_{\alpha\beta}h^{\alpha\beta}$.

It can be shown that using some elementary identities and some algebra, the Einstein tensor $G_{\alpha\beta}$ in Eq. (1.1) is reduced to:

$$G_{\alpha\beta} = \frac{1}{2}\left(\frac{\partial^2\bar{h}^l_\beta}{\partial x^\alpha \partial x^l} + \frac{\partial^2\bar{h}^m_\alpha}{\partial x^\beta \partial x^m} - \eta_{\alpha\beta}\frac{\partial^2\bar{h}^{lm}}{\partial x^l \partial x^m} - \Box^2\bar{h}_{\alpha\beta}\right) \ , \tag{1.7}$$

where $\Box$ is the d'Alembertian operator. This can be simplified by transforming into coordinates in which the divergence of the trace-reversed metric is zero. That is,

$$\frac{\partial\overline{h}^{\alpha\beta}}{\partial\beta} = 0 \ . \tag{1.8}$$

Now, if we make a transformation

$$x \to x' = x + \xi \ , \tag{1.9}$$

this implies that

$$g'_{\alpha\beta} = g_{\alpha\beta} - \frac{\partial\xi_\beta}{\partial x^\alpha} - \frac{\partial\xi_\alpha}{\partial x^\beta} \ , \tag{1.10}$$

and

$$h'_{\alpha\beta} = h_{\alpha\beta} - \frac{\partial\xi_\beta}{\partial x^\alpha} - \frac{\partial\xi_\alpha}{\partial x^\beta} \ . \tag{1.11}$$

We now choose the "Lorentz gauge":

$$\frac{\partial\overline{h}'_{\alpha\beta}}{\partial x'_\beta} = 0 \ , \tag{1.12}$$

so that from above equations, we get,

$$\Box^2\xi_\alpha = \frac{\partial\overline{h}_{\alpha\beta}}{\partial x_\beta} \ . \tag{1.13}$$

We see that the Einstein's equation, Eq. (1.1) reduces to:

$$\Box^2\bar{h}_{\alpha\beta} = -\frac{16\pi G}{c^4}T_{\alpha\beta} \ . \tag{1.14}$$

If we are far away from the source, $T_{\alpha\beta} = 0$ and the linearized vacuum Einstein's equations are:

$$\Box \bar{h}_{\alpha\beta} = 0 \ . \tag{1.15}$$

Eq. (1.15) gives us the wave equation and its plane wave solutions are known as GWs:

$$\overline{h}_{\alpha\beta} = A_{\alpha\beta} e^{ik_\gamma x^\gamma} \ . \tag{1.16}$$

Here $A$ is the amplitude and $k^\gamma$ is the wave vector.

### 1.1.2 Gravitational Wave Polarizations

To further simplify $\bar{h}_{\alpha\beta}$, we use the Transverse Traceless (TT) gauge. In this gauge:

1. $h_{00} = h_{0\alpha} = 0$ (Transverse)
2. $h^\alpha_\alpha = 0$ (Traceless)

Also, $\bar{h}^{TT}_{\alpha\beta} = h^{TT}_{\alpha\beta}$, so that a GW propagating in the $z$-direction will be expressed as:

$$h^{TT}_{\alpha\beta} = \begin{pmatrix} 0 & 0 & 0 & 0 \\ 0 & h_+ & h_\times & 0 \\ 0 & h_\times & h_+ & 0 \\ 0 & 0 & 0 & 0 \end{pmatrix} \ , \tag{1.17}$$

where $h_+$ and $h_\times$ are the two independent polarizations of the GW:

$$h_+ = A_+ e^{ik(ct-z)} \ , \tag{1.18}$$

$$h_\times = A_\times e^{ik(ct-z)} \ . \tag{1.19}$$

To visualize the two polarizations, consider a ring of test masses on the x-y plane. Fig. 1.1 depicts what happens when a GW passes through this plane. In the next section, we describe various kinds of GW sources.

## 1.2 Gravitational Wave Sources

Essentially, any body that has time varying quadrupole moment produces GWs. However, since the waves are extremely weak, the present-day detectors can only detect GWs from massive astrophysical systems. In this section, we discuss the different types of Gravitational Wave sources. All these sources emit GWs of different frequencies and last for different time-scales. The detectors have to identify these signals among the noise and so that we can study the properties of the source from it.

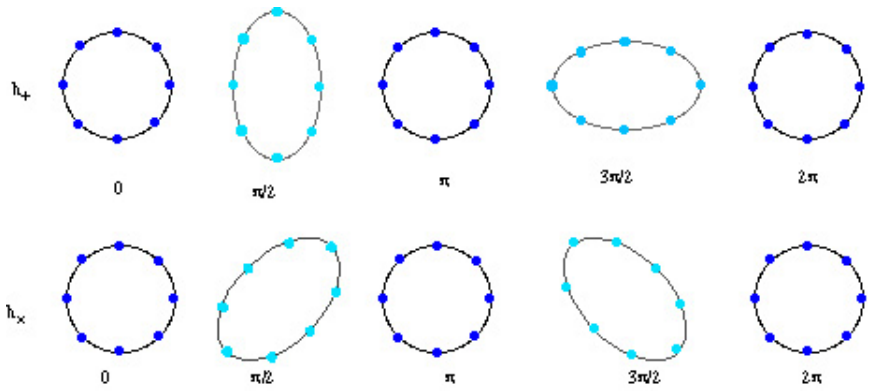


Figure 1.1: Motion of test masses in a ring as GW passes by. The two polarizations are 45° rotated with respect to each other. The ring first compresses in one direction and expands in another, and then visa versa as the Gw passes by. Image taken from [5]

### 1.2.1 Compact Binary Coalescences

Compact Binary Coalescences (CBCs) consist of two compact objects such as neutron stars (NSs) or black holes (BHs) orbiting around their center of mass. They emit energy and angular momentum in the form of GWs and hence their orbital separation decreases with time. CBCs are the most promising sources of GWs for second generation ground based detectors - in fact, the source of the very first detection GW150914, was a binary black hole (BBH) system [1].

There are several reasons for these sources to be considered important [6]. CBCs with total mass less than about 100 times that of the sun span a frequency range which is audible to the second generation ground based detectors. Another important reason is that these systems can be modelled to a high accuracy. That is, we have a very good idea from general theory of relativity of what the GW signal from these systems will look like. Essentially, we already know what we will be looking for in the strain data obtained from the detectors, and this greatly aids in the detection through optimal techniques like matched filtering [7], which will be discussed later. Another reason why we are so confident about CBCs is the event rates - we expect upto 40 NS-NS binary coalescences per year to be detected by advance LIGO (aLIGO), which is the second generation interferometric detector, once it reaches its full sensitivity. The event rate for NS-BH is 10 per year while for BH-BH 20 per year [8] (for updated event rates, please refer to [9]). That is almost a detection per week! Chapter 2 discusses the GWs emitted by CBCs in greater depth and Sec. 4.3 describes the data analysis work that undergoes in

detection and characterization of GWs from these systems.

### 1.2.2 Gravitational Collapse

Gravitational waves can be produced when a core of a massive star collapses to form a NS or a BH. This collapse results in Type II supernovae and are believed to be accompanied by long duration gamma-ray-bursts. Such events are expected to happen upto once every 10 years [10]. If the collapse is asymmetric in nature, it will produce GWs.

The main obstacle in detecting such burst sources is that we know very little about the physical processes that take place during such a collapse. Hence, we have very little information to use when we are modelling GW signals coming from these sources. The simulations that we rely on to model these waveforms are oversimplified and take a lot of assumptions. Nevertheless, they predict that the GWs emitted from these sources will lie well within the ground-based detectors, and could be detected.

### 1.2.3 Continuous Wave Sources

Continuous GW sources include rapidly spinning neutron stars that have axial asymmetry. These are typically the systems which emit GWs at a particular frequency for a long time. This frequency is determined by the frequency of the rotating system in consideration, and lies well within the aLIGO observable frequency.

However, the strain amplitude of the GWs from these sources is of the order of $10^{-25}$ on Earth [11]. This is orders of magnitude below the noise levels for aLIGO. In spite of this, it may be possible to detect such systems by collecting data for several months and over many cycles, since the effective amplitude is proportional to the square root of the number of cycles. This introduces modulations in the waveform due to the Earth's motion around the sun and the consequent Doppler effect, eliminating which is computationally expensive. Which is why there are programs such as Einstein@Home to aid the data analysis for such searches.

### 1.2.4 Stochastic Gravitational Wave Background

When there are multiple sources of GWs such that their signals overlap in both time and frequency and we cannot distinguish which signal belongs to which source, they have comparable strains. Examples of such sources could be binary white

dwarfs, which are plentiful in numbers in our galaxy itself. These would emit GWs at low frequencies. Such multiple sources would provide a GW background for low-frequency detectors such as the proposed space-based detector LISA (Laser Interferometer Space Antenna).

Even more interesting sources of GW background are the GWs produced shortly after the Big Bang [12] or during Inflation [13]. Electromagnetic cosmic background is limited to give information about the early universe only till the time when universe was not opaque. However, since gravitational interactions are very weak, matter is transparent for primordial GWs , and we can extract fundamental information about very early universe from these GWs.

## 1.3 Gravitational Wave Detectors

This section describes how the GW detectors actually detect the waves. The basic idea is that they detect the distortion in space-time due to GWs by the motion of test masses (masses that move along the geodesics of the curved space-time but their masses are small, so that they do not produce any curvature in space-time on their own). There are two basic kinds of detector designs - Resonant mass detector and Interferometer. We will only consider the latter in this thesis. In the GW interferometer, there is a monochromatic light source (in this case laser), whose light is separated and split into two halves of equal probability amplitude by a beam-splitter (see Fig. 1.2). One beam goes into an arm of the detector, while the another one goes into a second arm, which is orthogonal to the first. At the end of both the arms, we put totally reflecting mirrors. After reflection, the beams reunite at the beam splitter and a part of the interfered beam goes into the photodetector that measures its intensity.

Currently, there are several Earth based detectors spread across the globe -

1. LIGO Hanford and LIGO Livingston (USA): Each of these detectors has an arm length of 4Km.
2. VIRGO (Italy, under upgrade): Arm length of 3 Km.
3. GEO (Germany): Arm length of 600m
4. KAGRA (Japan, under construction): Arm length of 3 Km.
5. Einstein Telescope (planned): Arm length of 10 Km.
6. LIGO-INDIA (approved): Arm length of 4Km.

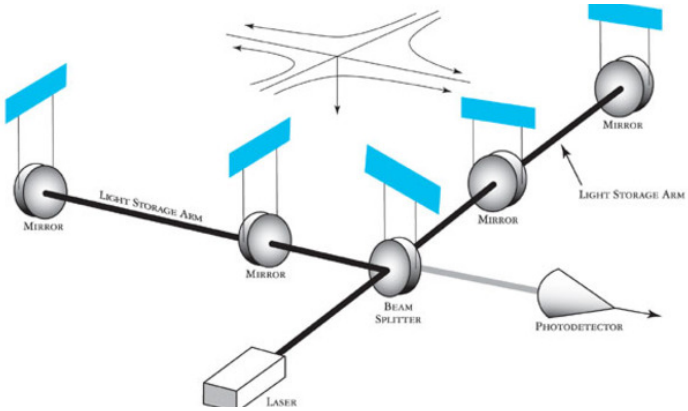


Figure 1.2: Basic design of the GW interferometer with Fabry-Perot cavity. Image taken form [14].

The LIGO detectors have the frequency bandwidth of a few Hz to a a few Mega Hz. Apart from these, there are plans to send interferometer in space - LISA for example, to detect low frequency GWs. Fig. 1.3.

### 1.3.1 Test Masses

As mentioned earlier, the detectors use freely falling test masses to detect the waves. The nature of the wave is such that it expands the space-time in one direction and contracts it in another. Suppose we have a grid of freely falling test masses put in a plane and a GW is incident on them. Let the plane of masses be characterized by $\hat{x}$ and $\hat{y}$ direction, and let the incident wave be incoming from the $\hat{z}$ direction. During the passage of the wave, a test mass $m_1$ at (1,0,0) will oscillate about its mean distance from the origin. Similarly, the test mass $m_2$ at (0,1,0) will oscillate about its mean distance from the origin. However, the polarization of the wave will ensure that these two things happen out of phase with respect to each other. That is, when $m_1$ is furthest away from the origin, $m_2$ is closest, and visa-versa.

The GW strength is characterized by its amplitude, which is measured by the detectors as:

$$h = \frac{2\Delta L}{L} \ , \tag{1.20}$$

where $L$ is the normal arm length of the interferometer, and $\Delta L$ is the change in the two arm lengths when a GW passes through the detector.

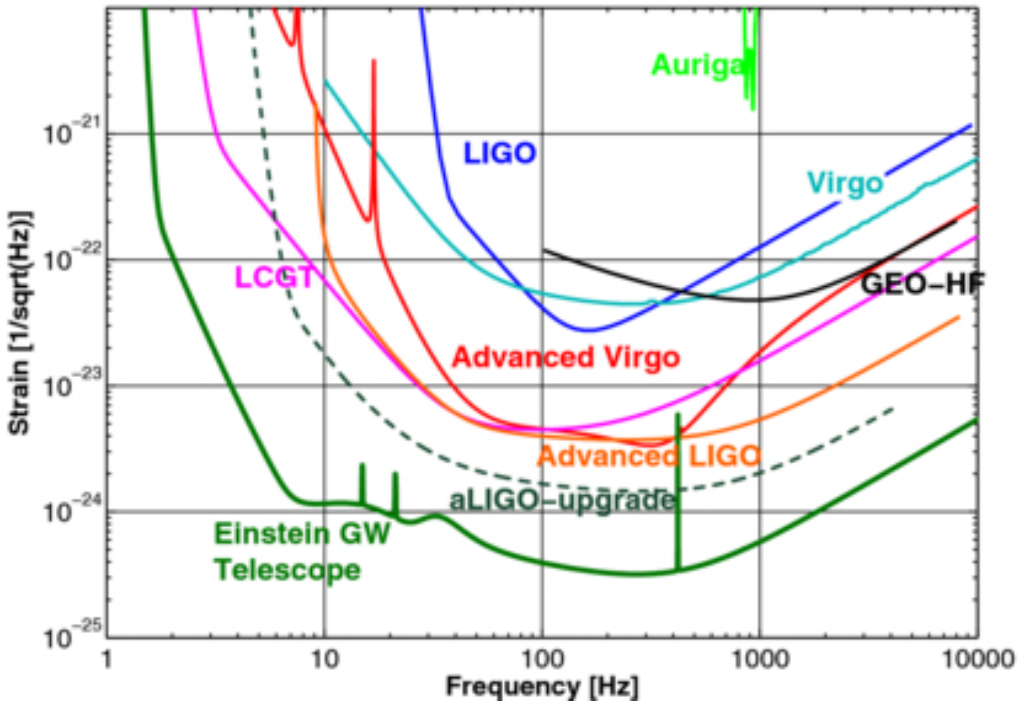


Figure 1.3: The frequency vs strain plots for different detectors. The plot shows the sensitivities of the detectors at different stages of their development. The image is taken from [14]

In the GW detectors involving interferometry, the mirrors at the end of each arm act as the test masses. Of course, they are not completely freely-falling, and suspensions in the design of the mirror mounts take care of that. However, these forces are static compared to the frequency of the GW, and as far as motion in the horizontal plane is concerned, they can be taken to be in free-fall.

### 1.3.2 Noise

Having defined the basic setup of the detector, we now look for the sensitivity at which a GW interferometer must work to have good chances of detection. A to-the-order calculation tells us that for a gravitational wave strength of $h_o \sim 10^{-21}$, the detectors with arm length 4Km need to measure $\Delta L$ of the order of $\Delta L \sim 10^{-18}$, which is smaller than the size of a proton by 1000 times! Hence, it becomes imperative that the detector experiences as little noise as possible. Following are some of the major sources of noise that limit the detector's sensitivity.

**Seismic noise**

The detector's chosen site is mostly a quiet site on the Earth. However, even for reasonably quiet site, the reduction of seismic noise required at a particular frequency is quite high. In addition, this reduction is not just to be done in the plane of the interferometer, but also in the vertical direction, since the noise in vertical direction may couple to the system placed in the horizontal plane. Thus, the mirrors in the arms (LIGO) have been suspended from a series of pendulums so as to make them as isolated from the seismic noise as possible. In addition, several hydraulic and electromagnetic systems have been installed to aid to the former design. These techniques also help in reduce the gravity gradient noise.

**Thermal noise**

The thermal noise associated with the mirror masses and the last stage of their suspensions is the most significant noise source at the low frequencies. In order to keep thermal noise as low as possible, the mechanical loss factors of the masses and pendulum resonances should be as low as possible. Further, the test masses must have a shape such that the frequencies of the internal resonances are kept as high as possible, must be large enough to accommodate the laser beam spot without excess diffraction losses, and must be massive enough to keep the fluctuations due to radiation pressure at an acceptable level.

**Quantum noise**

1. **Photon shot noise**: The origin of this noise lies in the fact that the laser is made up quanta of energy, photons. The output of the GW interferometer is set to a point in the fringes and is stabilized there by a feedback mechanism involving a photodiode. However, since the photoelectrons in the photo diode are distributed by Poisson distribution, which becomes Gaussian for large N with standard deviation equal to $\sqrt{N}$. Because of this, stabilization becomes difficult and this produces a limit to the sensitivities of the detector. The power is increased to overcome this difficulty.

2. **Radiation pressure**: To reduce the shot noise, we increase the power. However, a beam of photons that falls on the mirror and is reflected back itself exerts a pressure on the mirror. In addition, this pressure is not constant, otherwise, it could have simply be compensated by the mounting mechanisms of the mirror. However, since the number of photons that strike the mirror fluctuate (Gaussian distribution, as discussed before), the radiation pressure fluctuates in a stochastic manner. The effect of this pressure can

be reduced by decreasing the power (while keeping in mind the shot noise) or by increasing the mirror mass.

3. **The standard quantum limit**: We know that the shot noise varies with the power as $P^{-1/2}$ while the radiation pressure varies as $P^{1/2}$. The situation is conceptually similar to Heisenberg's Uncertainty Principle. When we use photons to detect the position of the mirrors, they impart non-deterministic radiation pressure. Thus, considering the combined effect of the shot noise and the radiation pressure, we see that there is only a limit till which it can be reduced.

#### Other noise sources

Apart from the major sources discussed above, there are various technical issues that can become important during sensitivity measurements. For example, the entire arm has to be in high vacuum in order to keep the noise induced by fluctuations in the index of refraction below the design sensitivity. The mirrors are to be polished to ultra-high accuracy to reduce the scattering effect. The fluctuations of the laser in power and in frequency must be kept under control to great accuracy.

## 1.4 GW150914 - First Direct Detection of Gravitational Waves

On September 14th, 2015 , both the aLIGO detectors at Hanford and Livingston, USA observed the GWs coming from a BBH system (dubbed GW150914) [1]. This was the first time that a direct detection of GWs was made. Before that, we only had indirect evidence of GWs through the Nobel-Prize winning work of Hulse and Taylor in 1974 on a binary pulsar system [2]. They had observed the puslar system for several years and found out that the orbit of the binary system is shrinking. This would mean that the system is loosing energy in the form of GWs. What Hulse and Taylor found out was in exact accordance with the prediction made by the General Theory of Relativity. Fig. 1.4 shows the accuracy to which the predictions by the theory match the observations made by Hulse and Taylor.

However, with the GW150914 event, we have the first direct GW detection. This not only confirmed the existence of GWs, but was another experimental evidence that the General Theory of relativity is correct [15]. Also, this was the first time we could detect a pair of BHs orbiting around each other.

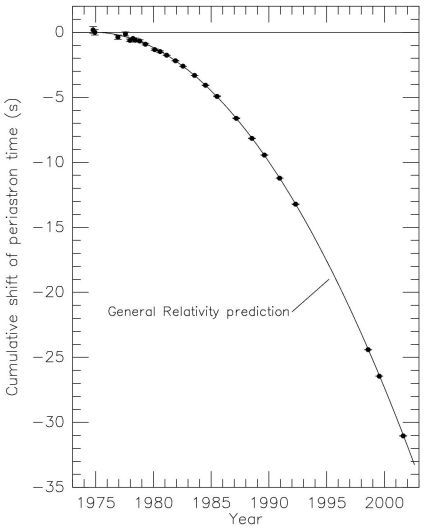


Figure 1.4: The Hulse-Taylor binary pulsar. The $x$ axis is the time (in years) and the $y$ axis is the cumulative shift in the periastron (point of least distance between the pulsars in their orbit)

The GW signal of GW150914 was a "chirp" signal. More about chirps is discussed in Chapter 2. It was created by the coalescence of two BHs of masses $29M\odot$ and $36M_{\odot}$. The merger took place 1.3 billion light years away and released energy of $3M_{\odot}$ in the form of GWs.

## 1.5 Gravitational Wave Astronomy

The first detection of GWs is bound to revolutionize the field of Astronomy. Until now, we only had access to the electromagnetic signals coming from the universe. Now, we have an entirely new and complementary spectrum in which we can make observations.

Electromagnetic (EM) waves are generated when a charge particle oscillates. However, since most of the universe is charge-neutral, we do not have access to information about the phenomenon occurring in deep space. GWs, on the contrary, are produced by acceleration of mass, and can provide us information in the areas we did not have access to with EM waves.

Also, GWs are weakly interacting with matter. So they would travel further before being affected by mass distributions. Essentially, we can probe much further into space, and much earlier into time, through GWs to understand physical processes happening out there.

With the advent of GW astronomy, we will be finally able to get the complete picture of our universe.

# Chapter 2

# Compact Binary Coalescences

As discussed in Sec. 1.2.1, the most promising sources of GWs for the present day ground based detectors are the CBCs. These comprise of NS-NS, BH-BH or NS-BH binary systems. As the binary system radiates GWs, their orbital separation decreases. Finally, they merge to form a final BH. Coalescence of a binary system can have physically three distinct phases:

1. **Inspiral**: In this phase, the compact objects are well separated. The binary system loses energy and angular momentum in the form of GWs and thus the separation between the compact objects decreases with time. Since the compact objects are far apart, we can use the Post-Newtonian (PN) approximation as the weak-field limit will be valid [16].

2. **Merger**: As the two compact objects are inspiraling towards each other, after one point, the two compact objects strongly interact with each other and the dynamics become unstable. The objects finally merge together to form a single BH, still radiating GWs .

3. **Ringdown**: The final deformed BH formed after the merger settles down into a stationary state, radiating GWs while removing its deformities.

The PN theory explains the inspiral phase with great accuracy, describing how a GW signal from a CBC would look like in this phase. However, we have to resort to the Numerical Relativity simulations for the merger phase. We have some analytical tools, known as BH perturbation theory [17], at our disposal to understand the ringdown phase. In practice, we can "stitch" the waveforms from these three phases into one, and have an accurate description of the entire Inspiral-Merger-Ringdown (IMR) waveform.

This chapter first discusses the various parameters that the GWs emitted by CBCs depend upon. Next, we look at mathematical formulation of GWs in the inspiral phase of a binary system. Finally, we see how a GW signal from a CBC looks like and briefly go through various ways in which it is being modelled.

## 2.1 Waveform Parameters

The GW signal from a CBC depends upon the following parameters:

1. Component masses of the binary system: $m_1$, $m_2$. We follow the convention that $m_1 \geq m_2$.
2. Spins are given by: $\mathbf{S}_1 = (Gm_1^2\chi_1/c)\mathbf{s}_1$ and $\mathbf{S}_2 = (Gm_2^2\chi_2/c)\,\mathbf{s}_2$, where $\chi_1$ and $\chi_2$ are the Kerr parameters and $\mathbf{s}_1$ and $\mathbf{s}_2$ are the unit vectors lying along $\mathbf{S}_1$ and $\mathbf{S}_2$. $\mathbf{S}_1$ and $\mathbf{S}_2$ are described by four angles $\theta_1$,$\theta_2$, $\phi_1$ and $\phi_2$ in an orbital triad. See Fig. 3.2.
3. Luminosity distance of the binary: $D_L$
4. Inclination angle, with respect to the line of sight: $\iota$
5. Right-Ascension: $\phi$
6. Declination: $\theta$
7. Polarization angle: $\psi$
8. Reference Phase: $\varphi_c$
9. Reference time of coalescence: $t_c$

So in total, there are 15 parameters on which the signal coming from a binary circular orbit depends. Out of the above mentioned parameters, the first 2 , i.e. masses and spins, are intrinsic variables, while the rest of them are extrinsic ones.

The Kerr parameters mentioned above are in the range [0,1], where $\chi = 0$ means non-spinning compact object while $\chi = 1$ means maximally spinning compact object. If the spin vectors are not aligned (or anti-aligned) to the orbital angular momentum $\mathbf{L}$, the orbital plane as well as the spin vectors precess around the total angular momentum. This results in modulations in the GW signal associated with these binaries, which is discussed in Sec. 2.3.

## 2.2 Binary System in a Circular Orbit

Consider a binary system with point masses $m_1$ and $m_2$ in a circular orbit on the $x$-$y$ plane. The orbital angular vector would point towards $z$ direction. In the center-of-mass frame, $m_1$ and $m_2$ will be at a distance $r_1$ and $r_2$ from the origin. Let the orbital separation be $a = r_1 + r_2$, the total mass $m = m_1 + m_2$ and the reduced mass $\mu = m_1 m_2/m$. This implies that $r_1 = am_2/m$ and $r_2 = am_1/m$.

In our study, we consider only circular orbit since the eccentricities of the orbit decay significantly by the time the GWs emitted by the binary become detectable by the ground-based detectors.

It is also important to note that the timescale over which the orbit shrinks is much more than the orbital period of the binary system. Hence, we can assume that $r_1$ and $r_2$ (and consequently the orbital separation $a$) remain constant over one orbit. The non-vanishing components of the quadrupole tensor, in terms of the orbital phase $\varphi = \omega t$, where $\omega$ is the angular velocity, are:

$$I_{xx} = \frac{1}{2}\mu a^2(1 + \cos 2\varphi) \ , \tag{2.1}$$

$$I_{xy} = \frac{1}{2}\mu a^2 \sin 2\varphi \ , \tag{2.2}$$

$$I_{yy} = \frac{1}{2}\mu a^2(1 - \cos 2\varphi) \ . \tag{2.3}$$

Taking the time derivatives twice,

$$\ddot{I}_{xx} = -2\mu a^2\omega^2 \cos 2\varphi \ , \tag{2.4}$$

$$\ddot{I}_{xy} = -2\mu a^2\omega^2 \sin 2\varphi \ , \tag{2.5}$$

$$\ddot{I}_{yy} = 2\mu a^2\omega^2 \cos 2\varphi \ . \tag{2.6}$$

Now, the observer on the $z$ axis at a distance $r$ from the origin will compute [3]:

$$h_{ij}^{TT} = -\frac{4G\mu a^2\omega^2}{c^4 r} \begin{pmatrix} \cos 2\varphi & \sin 2\varphi & 0 \\ \sin 2\varphi & -\cos 2\varphi & 0 \\ 0 & 0 & 0 \end{pmatrix} \ , \tag{2.7}$$

giving us the two polarizations:

$$h_+ = -\frac{4G\mu a^2\omega^2}{c^4 r} \cos 2\varphi \ , \tag{2.8}$$

$$h_\times = -\frac{4G\mu a^2\omega^2}{c^4 r} \sin 2\varphi \ . \tag{2.9}$$

We note that the frequency of the GW is twice that of the orbital frequency ($f_{GW} = 2f_{orbital} = \omega/\pi$). We invoke a change of variables $\nu = a\omega$, and we have :

$$\nu = (\pi G m f)^{1/3} = \sqrt{\frac{Gm}{a}} \ . \tag{2.10}$$

Here, $\nu$ is the orbital velocity and $\nu/c$ is sometimes known as PN expansion papameter. Now, the polarizations, in terms of $\nu$, become:

$$h_+ = -\frac{4G\mu}{c^2 r}\left(\frac{\nu}{c}\right)^2 \cos 2\varphi \ , \tag{2.11}$$

$$h_\times = -\frac{4G\mu}{c^2 r}\left(\frac{\nu}{c}\right)^2 \sin 2\varphi \ . \tag{2.12}$$

Phase can be written as:

$$\varphi = \omega t = \left(\frac{\nu}{c}\right)^3 \frac{c^3 t}{Gm} \ . \tag{2.13}$$

For an observer with the line of sight at an angle of inclination $\iota$ from the $z$ axis, the waveforms are:

$$h_+ = -\frac{2G\mu}{c^2 r}(1 + \cos^2 \iota)\left(\frac{\nu}{c}\right)^2 \cos 2\varphi \ , \tag{2.14}$$

$$h_\times = -\frac{4G\mu}{c^2 r}(\cos \iota)\left(\frac{\nu}{c}\right)^2 \sin 2\varphi \ . \tag{2.15}$$

These are the Newtonian waveforms. In practice, for real GW sarches we compute more accurate PN waveforms. For further reading, see [18, 19, 20].

### 2.2.1 Energy Loss and Luminosity

As the time progresses, the binary system will loose energy and angular momentum in the form of GWs, causing the orbit to shrink further and further. To calculate this energy loss, we take the third derivative of the quadrupole tensor:

$$\dddot{I}_{xx} = -\dddot{I}_{yy} = 4\frac{G}{c^5}\frac{\mu}{m}\left(\frac{\nu}{c}\right)^5 \sin 2\varphi \ , \tag{2.16}$$

$$\dddot{I}_{xy} = 4\frac{G}{c^5}\frac{\mu}{m}\left(\frac{\nu}{c}\right)^5 \cos 2\varphi \ . \tag{2.17}$$

Using these time derivatives, the GW Luminosity is given by:

$$L_{GW} = \frac{32}{5}\frac{c^5}{G}\eta^2\left(\frac{\nu}{c}\right)^{10} \ , \tag{2.18}$$

where $\eta = \mu/m$ is called the *symmetric mass ratio*. The Newtonian energy loss is given by:

$$E = \frac{1}{2}m_1\nu_1^2 + \frac{1}{2}m_2\nu_2^2 - \frac{Gm_1m_2}{a} \ , \tag{2.19}$$

$$= -\frac{1}{2}\mu\nu^2 \ . \tag{2.20}$$

### 2.2.2 Time Until Coalescence

The luminosity is given by $L_{GW} = -dE/dt$. Now, using the results obtained in the previous section, we have :

$$\Rightarrow \frac{d(\nu/c)}{dt} = \frac{32\eta}{5}\frac{c^3}{Gm}\left(\frac{\nu}{c}\right)^9 \ . \tag{2.21}$$

The time until coalescence, $\tau_c$, can be found by integrating Eq. (2.21):

$$\int_{\nu_0/c}^{\infty} \frac{d(\nu/c)}{(\nu/c)^9} = \frac{32\eta}{5}\frac{c^3}{Gm}\int_0^{\tau_c} dt \ , \tag{2.22}$$

where we start with some initial frequency. Since the correction is very small and can be ignored, we take the upper limit to be infinity, rather than choosing the cutoff frequency for which the binary travels at the speed of light, so as to make the calculations simple. Now, the time till coalescence is given by:

$$\tau_c = \frac{5}{256\eta}\frac{Gm}{c^3}\left(\frac{\pi G m f_0}{c^3}\right)^{-8/3} \ , \tag{2.23}$$

where $f_0$ is the starting frequency.

### 2.2.3 Phase Evolution

Since the orbital separation is reducing with time due to the emission of GWs, the phase $\varphi$ will not increase uniformly with time. To compute the phase evolution, we introduce two dimensionless functions:

1. Energy function: $\mathbb{E}$, which is related to the energy $E$ by:

$$E(\nu) - mc^2 = mc^2\mathbb{E}(\nu) \ . \tag{2.24}$$

2. Flux function: $\mathbb{F}$, which is related to the luminosity by:

$$L_{GW}(\nu) = \frac{c^5}{G}\mathbb{F}(\nu) \ . \tag{2.25}$$

The time $t$ at which the binary system reaches the orbital velocity $\nu$ is given by:

$$t(\nu) = t_c + \frac{Gm}{c^3}\int_{\nu}^{\nu_c} \frac{1}{\mathbb{F}}\frac{d\mathbb{E}}{d\nu}d\nu \ , \tag{2.26}$$

and the orbital phase is given as:

$$\varphi(\nu) = \varphi_c + \int_{\nu}^{\nu_c} \left(\frac{\nu}{c}\right)^3 \frac{1}{\mathbb{F}}\frac{d\mathbb{E}}{d\nu}d\nu \ . \tag{2.27}$$

### 2.2.4 Newtonian Chirp

Now that we have $\varphi(\nu)$ and $t(\nu)$, the waveform can be written in terms of $\nu$ as:

$$h_+(t(\nu)) = -\frac{2G\mu}{c^2 r}(1+\cos^2\iota)\left(\frac{\nu}{c}\right)^2 \cos 2\varphi(\nu) \ , \tag{2.28}$$

$$h_\times(t(\nu)) = -\frac{4G\mu}{c^2 r}(\cos\iota)\left(\frac{\nu}{c}\right)^2 \sin 2\varphi(\nu) \ . \tag{2.29}$$

The above two equations represent the "chirp" waveform - the frequency and amplitude both increase as the orbit decays. For the Newtonian case, we have:

$$\mathbb{E} = -\frac{1}{2}\eta\left(\frac{\nu}{c}\right)^2 \ , \tag{2.30}$$

and

$$\mathbb{F} = \frac{32}{5}\eta^2\left(\frac{\nu}{c}\right)^{10} \ . \tag{2.31}$$

This yields us $\varphi(\nu)$ and $t(\nu)$ through Eqs. (2.26) and (2.27). Subsequently, we can compute the time-derivative of the GW frequency:

$$\frac{df}{dt} = \frac{96}{5}\pi^{8/3}\eta\left(\frac{Gm}{c^3}\right)^{5/3} f^{11/3} = \frac{96}{5}\pi^{8/3}\left(\frac{G\mathcal{M}}{c^3}\right)^{5/3} f^{11/3} \ , \tag{2.32}$$

where $\mathcal{M} = \eta^{3/5}m = (m_1 m_2)^{3/5}(m_1+m_2)^{-1/5}$ is called the *chirp mass*. The frequency evolution depends on the companion masses only through the chirp mass. Moreover, even the GW waveforms depend only on this combination of the companion masses:

$$h_+(t) = -\frac{G\mathcal{M}}{c^2 r}\frac{1+\cos^2\iota}{2}\left(\frac{c^3(t_c-t)}{5G\mathcal{M}}\right)^{-1/4}\cos\left[2\varphi - 2\left(\frac{c^3(t_c-t)}{5G\mathcal{M}}\right)^{5/8}\right] \ , \tag{2.33}$$

$$h_\times(t) = -\frac{G\mathcal{M}}{c^2 r}\cos\iota\left(\frac{c^3(t_c-t)}{5G\mathcal{M}}\right)^{-1/4}\sin\left[2\varphi - 2\left(\frac{c^3(t_c-t)}{5G\mathcal{M}}\right)^{5/8}\right] \ . \tag{2.34}$$

In the next section we will see what kind of GW signals are produced from CBCs.

## 2.3 Waveforms for Compact Binary Coalescences

A typical GW waveform from a coalescing binary system is shown in Fig.2.3 for a BBH.

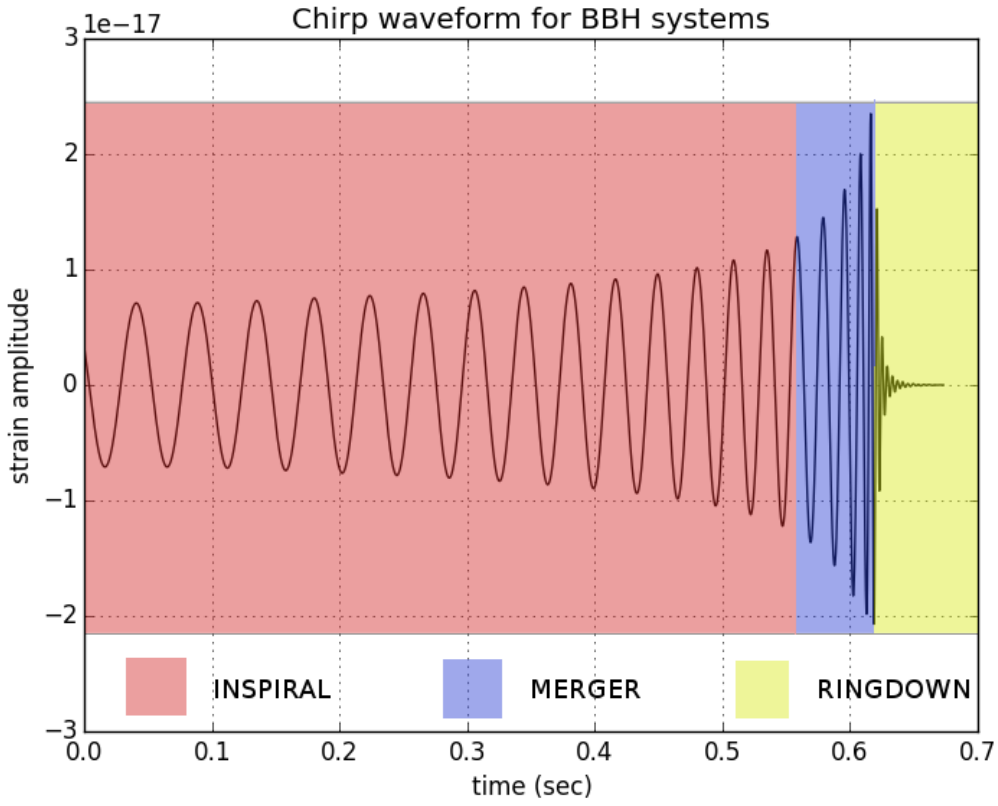


Figure 2.1: A typical chirp waveform showing the three different phases of coalescence - Inspiral, Merger and Ringdown.

We can notice that during the inspiral phase, as time increases, the frequency and the amplitude of the waveform increases. During the merger phase, the rise in the amplitude is significant - the binary system can release upto some percentage of their total mass as GW while merging and forming a bigger BH. Finally, we can see the damping down of the waveform during the ringdown phase, where the final BH settles down. There are no sharp boundaries between the phases, although that is what has been depicted in the figure for the sake of clarity.

We know from the beginning of the chapter that the waveform depends on various parameters. To see an example of that, we have three waveforms in Fig. 2.2 for a binary system with each of the component masses equal to $15M_{\odot}$ where $M_{\odot}$ is the mass of the Sun. All figures describe only the inspiral part, with the lower cutoff frequency 20 Hz. In the first case, the compact objects in the binary system are not spinning and there is no modulation in the waveform. In the second case, they are spinning; however, since their spins are aligned with the orbital angular momentum, they are not precessing. In the third case, the spins are not aligned with the angular momentum and hence the orbital plane and the spins are precessing, and we can clearly see the modulations in the waveform as a result.

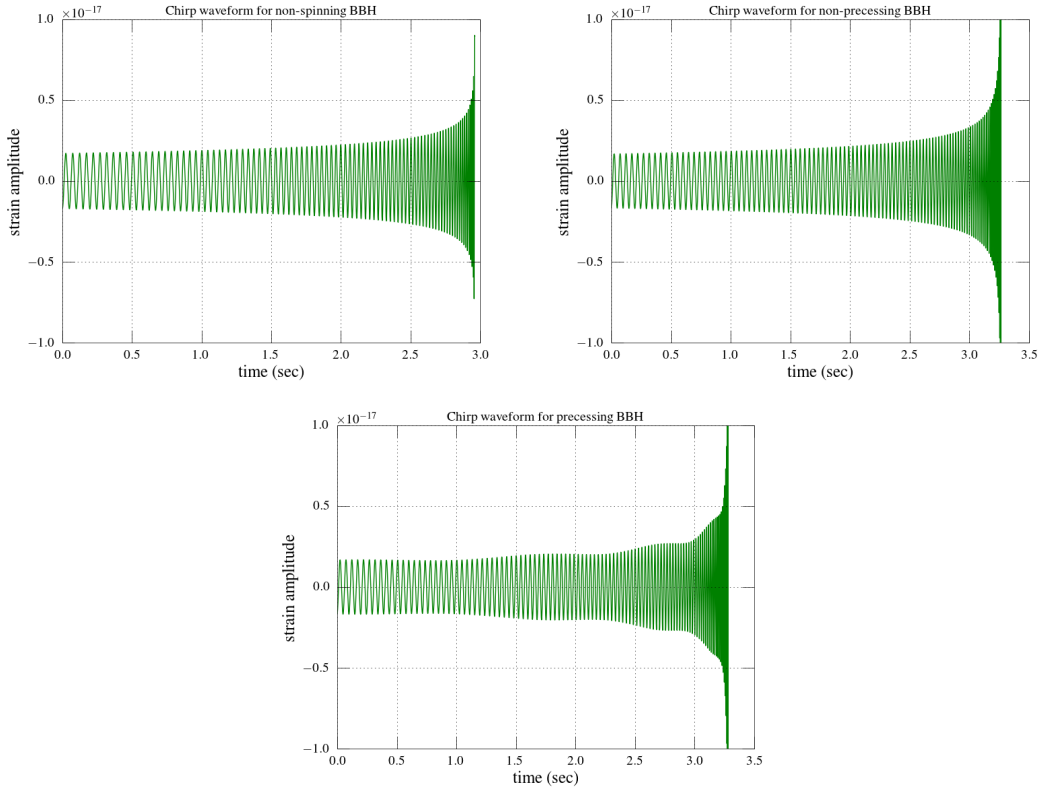


Figure 2.2: The first figure describes the waveform for a non-spinning BBH, the second figure describes the waveform for non-precessing BBH while the third figure describes the waveform for a precessing BBH.

If the masses of the compact objects are higher, the length of the inspiral part, with reference to a starting frequency, will be shorter. This is because binary systems with higher mass tend to release energy through GWs quickly as compared to the lower mass counterparts. So the time taken to reach the merger phase is less.

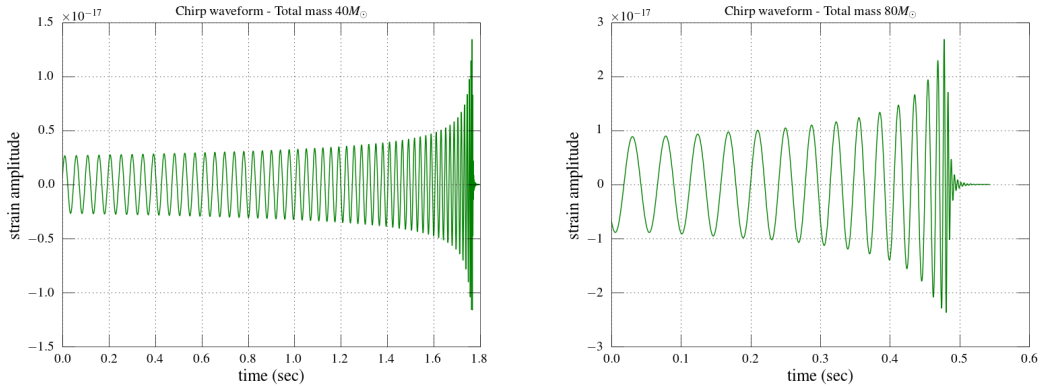


Figure 2.3: The left panel describes the waveform for a BBH with total mass $40M_\odot$, while the one on the right describes the waveform for a BBH with total mass $80M_\odot$.

Given a binary system and its parameters, it is not a trivial task to model the full IMR waveform. The following subsections discuss what are the current techniques to compute a desired waveform.

### 2.3.1 Numerical Relativity Simulations

Numerical Relativity (NR) has been remarkably successful in the recent years to simulate binary BH systems and generate their GW waveforms. It specially helps in predicting the behavior of the binary during the merger phase, for which we do not have much analytical tools. Simulation platforms like SpEC (Spectral Einstein Code) [21] have been extensively used to generate GW waveforms for various binary systems.

### 2.3.2 Waveform Approximants

As accurate as they may be, NR simulations are computationally very expensive - a high quality waveform may require months to be generated. For reasons that we will discuss later in Sec. 4.3, we require large number of waveforms for

detection and parameter estimation. Hence, we cannot rely on just NR waveforms for these purposes. Consequently, we have developed several mathematical models for the waveforms. These models span a wider volume in the parameter space (as compared to just one point in case of a NR waveform) and have been calibrated using NR waveforms so that they generate accurate waveforms. Some of these models generate waveforms in time domain, while others in frequency domain. All of them are coded in LIGO Algorithm Library's LALSUITE [22]. Some of the approximants covered in this thesis are described in the following paragraphs.

### SpinTaylorT4

To compute a waveform, this approximant solves 14 first order coupled differential equations. This is a time domain waveform and incorporates spin and precession effects of the component masses [23]. However, this is inspiral-only waveform, i.e. it generates only the inspiral part of the waveform.

### Reduced Spin

This is a frequency-domain waveform model that is characterized by 3 parameters - the masses and a reduced spin parameter $\chi = \chi_s + \delta\,\chi_a - 76\,\eta/113\,\chi_s$, where $\delta = (m_1 - m_2)/m$, $\chi_s = (\chi_1 + \chi_2)/2$ and $\chi_a = (\chi_1 - \chi_2)/2$. Here $\chi_1$ and $\chi_2$ are the z-components of the Kerr parameters of component masses and $m = m_1 + m_2$. This waveform model is inspiral-only [24].

### Phenomenological models: IMRPhenomD

For detection and parameter estimation of GWs, we require waveform models in frequency domain and with low computational cost. Phenomenological models have been proposed that stitch together PN waveforms and NR simulations to span all the three phases of coalescence of a binary. This is a 3 parameter waveform family that depends upon $m$, $\eta$ and an effective spin parameter $\chi_{eff} = (1+\delta)\,\chi_1/2 + (1-\delta)\,\chi_2/2$. This model made use of simple analytical ansätze for the phase and amplitude of the PN-NR hybrids. Later on these ansätze were suitably modified to make smooth transitions between their inspiral, merger and ringdown forms, and improved the accuracy of the model [25]. The most recent IMRPhenomD model has improvised on several features as compared to its predecessors. It has also been calibrated using several NR waveforms and thus has a wide range of applicability in terms of the parameter space it covers.

**Effective One-Body approximation: SEOBNRv2 and SEOBNRv3**

These waveform model use the Effective-One-Body (EOB) method to solve the two body problem in general relativity. In the Spin EOB framework, the conservative dynamics of two compact objects of masses $m_1$ and $m_2$ and spins $\mathbf{S}_1$ and $\mathbf{S}_2$ is mapped into the dynamics of an effective particle of mass $\mu = m_1 m_2/(m_1+m_2)$ and spin $\mathbf{S}_*$ moving in a deformed Kerr metric with mass $m = m_1+m_2$ and spin $S_{\rm Kerr} = \mathbf{S}_1 + \mathbf{S}_2$. Over a decade of improvements and developments, EOB model has now become the most accurate IMR waveform model for spinning and non-precessing binaries [26, 27]. This approximant aids in modelling the last stages of inspiral, merger and ringdown. Since SEOBNRv2 itself is computationally expensive, we use its reduced-order-modelling format (SEOBNRv2-ROM-DoubleSpin).

SEOBNRv3 is an inspiral-merger-ringdown model for precessing binaries [28]. SEOBNRv3 is mainly built upon its non-precessing version SEOBNRv2, and employs the precessing convention introduced by Buonanno, Chen, and Vallisneri [29] and uses a non-inertial *precessing source frame* to describe the dynamics of the system.

# Chapter 3

# Spin-Orbit Resonances in Black Hole Binaries

The GW that is produced from BBH depends on whether the BHs are spinning. The modulation in waveform also depends on how fast the masses are spinning. Moreover, if the spin vectors are not aligned with the orbital angular momentum, they will precess about it, bringing more modulations to the GW waveform.

This chapter discusses about such highly spinning and precessing BBH. In the first section, the dynamics of such systems is discussed. In the next section, we discuss certain equilibrium configurations that may exist in some of these binary systems.

## 3.1 Dynamics of Precessing Binary Black Hole system

In the parameter space for a BBH system, there are 8 intrinsic variables: the masses (2), the magnitudes of the spins (2) and the directions of the spins (4 angles). We have already mention the masses and the spins in Sec.(2.1). Similarly, the orbital angular momentum is $\mathbf{L} = (Gm^2\eta/c\sqrt{x})\hat{\mathbf{L}}$ where $m = m_1 + m_2$ is the total mass, $\eta = (m_1 m_2/m^2)$, $x = (Gm\omega/c^3)^{2/3}$, $\omega$ is the angular velocity and $\hat{\mathbf{L}}$ is the unit vector along $\mathbf{L}$.

The total angular momentum is given by :

$$\mathbf{J} = \mathbf{L} + \mathbf{S}_1 + \mathbf{S}_2 \ , \tag{3.1}$$

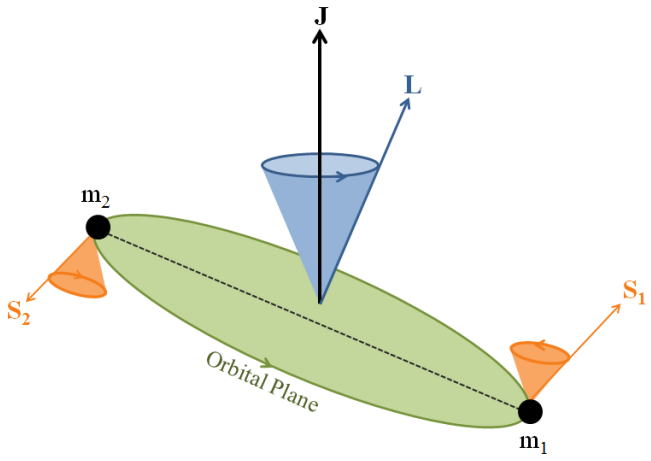


Figure 3.1: A schematic showing the precession of a binary system. Spins $\mathbf{S}_1$, $\mathbf{S}_2$ and $\mathbf{L}$ precess around the total angular momentum $\mathbf{J}$ [30]

.

and the vectors $\mathbf{s}_1$, $\mathbf{s}_2$ and $\hat{L}$ all precess around $\mathbf{J}$. For two point masses which are spinning, the precession equations are [31, 32]:

$$\dot{\mathbf{S}}_1 = \mathbf{\Omega}_1 \times \mathbf{S}_1 \ , \tag{3.2}$$

$$\dot{\mathbf{S}}_2 = \mathbf{\Omega}_2 \times \mathbf{S}_2 \ , \tag{3.3}$$

where $\mathbf{\Omega}_1$ and $\mathbf{\Omega}_2$ are the precession frequencies of $\mathbf{S}_1$ and $\mathbf{S}_2$, defined for a circular orbit for two masses separated by a distance $r$ as:

$$\mathbf{\Omega}_1 = \frac{1}{2r^3}\left[\left(2+\frac{3}{q}-\frac{3(q\mathbf{S}_2+\mathbf{S}_1)\cdot\mathbf{L}}{qL^2}\right)\mathbf{L}+\mathbf{S}_2\right] \ , \tag{3.4}$$

$$\mathbf{\Omega}_2 = \frac{1}{2r^3}\left[\left(2+3q-\frac{3(\mathbf{S}_1+q\mathbf{S}_2)\cdot\mathbf{L}}{L^2}\right)\mathbf{L}+\mathbf{S}_1\right] \ . \tag{3.5}$$

Here $q = m_1/m_2$ is the mass ratio.

There are three timescales involved in the evolution of BBH systems [33]. These are the timescales associated with the orbital ($\tau_{orb}$), precessional ($\tau_{pre}$) and inspiral ($\tau_{rr}$) dynamics of the system. They are related to each other by the following inequality:

$$\tau_{orb} \ll \tau_{pre} \ll \tau_{rr} \ , \tag{3.6}$$

which means that the two BHs will make many orbits around each other in the same time as the orbital angular momentum ($\mathbf{L}$) precesses once around the total

angular momentum (**J**). Similarly, **L** would have made many precessing orbits around **J** in the same time as the orbit size would have shrunk.

It is to be noted that **J** changes with time due to the radiation reaction (as **L** changes). However, in the point mass approximation, the magnitude of spins $|\mathbf{S}_{1,2}|$ remains constant. If the BBH system did not emit GWs , the orbits will not shrink and **J** would remain constant.

## 3.2 Equilibrium Configurations

In 2004, Schnittman observed that for spinning and precessing BH binaries, there are some equilibrium configurations, in which **L**, $\mathbf{S}_1$ and $\mathbf{S}_2$ lie in a common plane [33]. These configurations are called "spin-orbit resonant" configurations since in the absence of radiation reaction, **L**, $\mathbf{S}_1$ and $\mathbf{S}_2$ precess around **J** at a constant frequency. Fig. 3.2 shows the coordinate framework that is used in this thesis. The three vectors, namely **L**, $\mathbf{S}_1$ and $\mathbf{S}_2$, determine the axes as follows: $\hat{\mathbf{e}}_z$ is along **L**; $\mathbf{S}_{1,2}$ make angles $\theta_{1,2}$ with **L** and their projections on $x-y$ plane make angles $\phi_{1,2}$ with $\hat{\mathbf{e}}_x$, respectively; we set $\phi_1 = 0$.

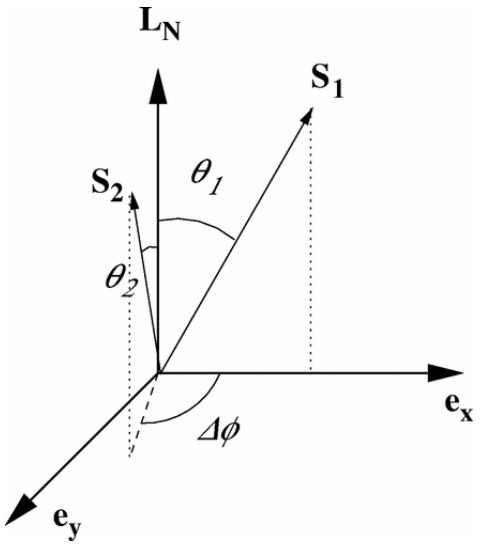


Figure 3.2: Reference frame used to describe the spin vectors: **L** is along the z-axis. $x$ axis is such that it makes an angle of $0^\circ$ with the projection of $\mathbf{S}_1$ on $x-y$ plane. This figure is taken from [33].

Given the spin magnitudes $|\mathbf{S}_{1,2}|$, that do not change over time, we end up having 4 independent dynamical variables for determining the orientation of the binary system: $L$, $\theta_1$, $\theta_2$ and $\Delta\phi = \phi_2 - \phi_1$.

As mentioned earlier, there are configurations in this coordinate framework in which $L$, $\theta_1$, $\theta_2$ and $\Delta\phi$ remain fixed in the absence of radiation reaction. The individual vectors may vary with time as seen from another fixed inertial coordinate framework.

The most trivial solutions are the ones in which $\mathbf{S}_{1,2}$ are collinear with $\mathbf{L}$ (i.e. $\cos\theta_1 = \pm 1$ and $\cos\theta_2 = \pm 1$). However, there are more equilibrium configurations when the spins and angular momentum are precessing, and are given when:

$$\frac{d}{dt}(\mathbf{S}_1 \cdot \mathbf{S}_2) = 0 \ , \tag{3.7}$$

$$\Rightarrow \left[\frac{m_2}{m_1} - \frac{m_1}{m_2} + \frac{(\mathbf{S}_1 - \mathbf{S}_2)\cdot \mathbf{L}}{L^2}\right] \mathbf{S}_2 \cdot (\mathbf{L} \times \mathbf{S}_1) = 0 \ . \tag{3.8}$$

Eq. (3.8) means that the scalar triple product $\mathbf{S}_2 \cdot (\mathbf{L} \times \mathbf{S}_1)$ should vanish for all times. That is, $\mathbf{S}_1$, $\mathbf{S}_2$ and $\mathbf{L}$ should be coplanar for all times. This means we have to find the simultaneous solutions for the following two equations:

$$\mathbf{S}_2 \cdot (\mathbf{L} \times \mathbf{S}_1) = 0 \ , \tag{3.9}$$

and

$$\frac{d}{dt}[\mathbf{S}_2 \cdot (\mathbf{L} \times \mathbf{S}_1)] = 0 \ . \tag{3.10}$$

Also, the scalar triple product, in terms of the four independent variables, can be expressed as:

$$\mathbf{S}_2 \cdot (\mathbf{L} \times \mathbf{S}_1) = S_1 S_2 L \sin\theta_1 \sin\theta_2 \sin\Delta\phi \ . \tag{3.11}$$

This, along with Eq. (3.9), provides the condition:

$$S_1 S_2 L \sin\theta_1 \sin\theta_2 \sin\Delta\phi = 0 \ . \tag{3.12}$$

The above equation generates two classes of solutions: $\Delta\phi = 0°$ and $\Delta\phi = 180°$. Now, combining Eqs. (3.9),(3.10),(3.4) and (3.5) we get:

$$(\mathbf{\Omega_1} \times \mathbf{S_1}) \cdot [\mathbf{S_2} \times (\mathbf{L} + \mathbf{S_1})] = (\mathbf{\Omega_2} \times \mathbf{S_2}) \cdot [\mathbf{S_1} \times (\mathbf{L} + \mathbf{S_2})] \ , \tag{3.13}$$

which is an equation in terms of the parameters $L$, $\theta_1$, $\theta_2$ and $\Delta\phi$. This allows us to calculate $\theta_2$ given $m_1$, $m_2$, $\chi_1$, $\chi_2$, $L$, $\Delta\phi$ and $\theta_1$. These configurations are dominant when the mass ratio $q \in [1, 3]$ and $\chi_1, \chi_2 \in [0.5, 1]$ [33].

The following Fig. 3.3 describes the two families of $\theta_1$-$\theta_2$ relations for various spin magnitudes for masses $m_1 = 11M_\odot$ and $m_2 = 9M_\odot$. We plot Schnittman's equilibrium solutions of $\theta_2$ as a function $\theta_1$. Also, different curves are for different orbital separations: $x = 1/1000,\ 1/500,\ 1/250,\ 1/100$ and $1/10$, where $x = 1/1000$ is equivalent to an orbital separation of $r = 500R_s$. Here $R_s$ is the Schwarzschild radius $R_s = 2Gm/c^2$. Here, we considered BHs in the binary to have the spins $\chi_1 = \chi_2 = \chi = 0.5, 0.75$ and $0.98$. Note that similar plots are presented in [33] and [30] for maximally spinning BHs in Fig. 2,3 and Fig. 2, respectively. In this thesis, we are presenting these solutions for submaximally spinning BHs for the first time. We see that the solutions for sub-maximally spinning BBH are different than those for maximally spinning cases. For $\Delta\phi = 0^\circ$ case, we get multiple branches even at smaller separations as the spins are reduced. For $\Delta\phi = 180^\circ$, the range of solutions becomes more shallow.

In the next section, we briefly describe the important astrophysical implications of Spin-Orbit resonances.

## 3.3 Astrophysical Implications of Spin Orbit Resonant Binaries

The spin orbit resonances have important astrophysical implications. It has been observed that during the later stages on inspiral for certain such configurations, $\mathbf{s}_1 \cdot \mathbf{s}_2$ approaches unity [34]. Binaries that are near these equilibrium configurations can get locked and liberate around them during their inspiral. For comparable mass supermassive BH binaries, spin-alignment during late inspiral phase would mean that the recoil velocity experienced by the resultant BH formed after merger will not be large [34, 35]. Thus, the remnants will remain in the galaxies that are hierarchically formed from the merger of smaller galaxies. It was recently shown by Gerosa et al. that comparable stellar mass BH binary systems tend to lie in a resonant plane by the time their GWs enter the frequency band of aLIGO [36].

Therefore, it will be interesting to see if the binaries in these configurations can be detected by the advanced GW detectors. Currently, the detection pipelines used by LSC employ only non-spinning and non-precessing waveforms for CBC searches. In this thesis, we are testing the performance of these template banks in detecting spin-orbit resonant binaries.

The next chapter describes the data analysis tools that we have used for this investigation.

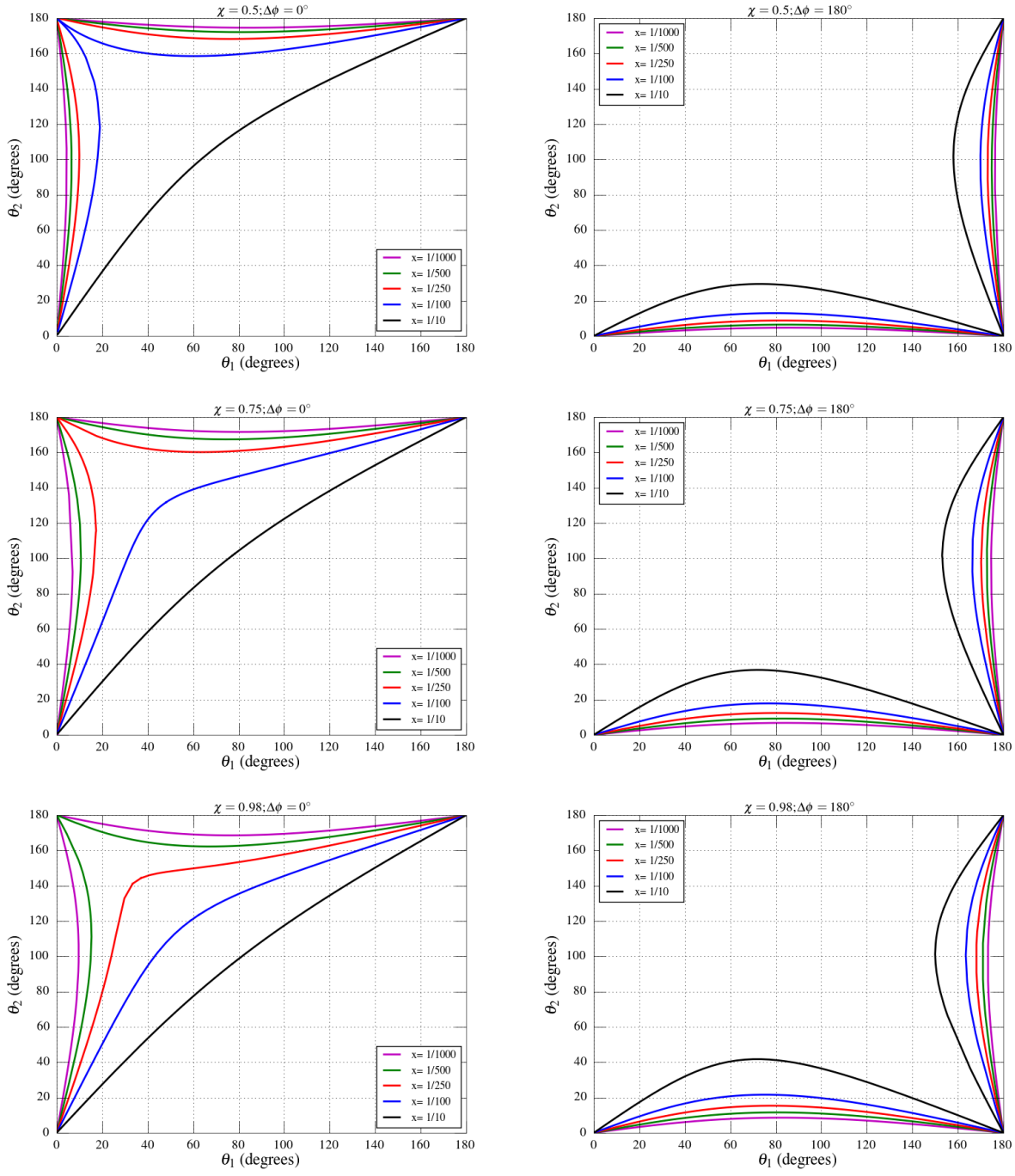


Figure 3.3: Equilibrium solution for $\theta_2$ as a function of $\theta_1$. The plots are for the masses $m_1 = 11M_\odot$ and $m_2 = 9M_\odot$ both having the same Kerr parameter $\chi$. The left panel is for $\Delta\phi = 0°$ family, while the right panel is for $\Delta\phi = 180°$ family. The top panel describe the solutions for $\chi = 0.5$, the middle for $\chi = 0.75$, and the bottommost for $\chi = 0.98$.

# Chapter 4

# Gravitational Wave Data Analysis

The data we get from the inferometric LIGO-like detectors is a discretized time series in strain. Let the strain data from the detector be given by $s(t)$. This data consists of two components: the random noise $n(t)$ and a possible GW signal $h(t)$, so that:

$$s(t) = n(t) + h(t) \ . \tag{4.1}$$

Since GW signals are extremely weak signals, even with the sensitivity of current detectors, these are buried inside a lot of noise and we have to extract it out. The optimal technique of Matched Filtering maximizes the signal-to-noise ratio (SNR), assuming that the signal is present in the data stream.

## 4.1 Matched Filtering

This section contains the details about the Matched Filtering technique of extracting signals from noisy data [7]. The basic idea of matched filtering is used in many signal extraction process, including radio engineering. Using this technique, we can detect $h(t) \leq n(t)$ if we have some idea of the signal we are looking for.

### 4.1.1 Power Spectral Density

Consider a time series data $x(t)$ having the probability distribution $p_x$ for the value of $x$ at time $t$. The expectation value of $x$ at that time is given as:

$$< x >= \int x p_x(x) dx = \lim_{T\to\infty} \frac{1}{T} \int_{-T/2}^{T/2} x(t) dt \ . \tag{4.2}$$

If the distribution function of the process does not alter with time then it is called a stationary random process. Now, consider a signal with zero mean (i.e.

$< x >= 0$). The power is defined as :

$$< x^2 >= \lim_{T\to\infty} \frac{1}{T} \int_{-T/2}^{T/2} x^2(t)dt \ . \tag{4.3}$$

If the signal $x(t)$ is present in the interval $[-T/2, T/2]$, we can define a windowed signal as:

$$x_T(t) = \begin{cases} x(t) & -T/2 < t < T/2 \ , \\ 0 & \text{otherwise} \end{cases}$$

so that :

$$\begin{aligned} < x^2 > &= \lim_{T\to\infty} \frac{1}{T} \int_{-\infty}^{\infty} x_T^2(t)dt \ , & (4.4)\\ &= \lim_{T\to\infty} \frac{1}{T} \int_{-\infty}^{\infty} |\tilde{x}_T^2(f)|df \ , & (4.5)\\ &= \lim_{T\to\infty} \frac{2}{T} \int_{0}^{\infty} |\tilde{x}_T^2(f)|df \ , & (4.6)\\ &= \int_{-\infty}^{\infty} S_x(f)df \ . & (4.7) \end{aligned}$$

Here $S_x(f)$ is the one-sided *power spectral density* (PSD), since we have removed the negative frequency components. In the above derivation, we have used the Parseval's theorem:

$$\int_{-\infty}^{\infty} |x_T^2(t)|^2 dt = \int_{-\infty}^{\infty} |\tilde{x}_T(f)|^2 df \ . \tag{4.8}$$

Thus, the PSD of a stationary random process $x(t)$ is given as:

$$S_x(f) = \lim_{T\to\infty} \frac{2}{T} \left| \int_{-T/2}^{T/2} x(t)\, e^{-2\pi i f t} dt \right|^2 \ . \tag{4.9}$$

It depicts the frequency composition of the power of that signal. The PSD for a stationary process is also two times the Fourier transform of the autocorrelation function, which is given as:

$$R_x(t) =< x(t)x(t+\tau) > \ . \tag{4.10}$$

We define the noise weighted inner product $(a, b)$ of two time series $a(t)$ and $b(t)$ as:

$$(a, b) = 4\, Re \int_0^{\infty} \frac{\tilde{a}(f)\tilde{b}^*(f)}{S(f)} df \ . \tag{4.11}$$

Also, we define the match between $a$ and $b$ as $(a|b)$:

$$(a|b) = (a', b') \ , \tag{4.12}$$

where

$$a' = \frac{a}{\sigma_a} \ , \tag{4.13}$$

and

$$\sigma_a = \sqrt{(a|a)} \ . \tag{4.14}$$

### 4.1.2 Detection Statistic and Bayes's Theorem

For the given strain data $s(t)$, we have two hypotheses:

1. Null Hypothesis $\mathcal{H}_0 : \ s(t) = n(t)$
2. Alternative Hypothesis $\mathcal{H}1 : \ s(t) = n(t) + h(t)$

where $s(t), n(t)$ and $h(t)$ are the strain data, noise and signal, respectively. We wish to distinguish between the two hypotheses using Bayes's theorem.

We denote the probability of the event $\mathcal{A}$ happening by $P(\mathcal{A})$ and for the event $\mathcal{B}$ happening by $P(\mathcal{B})$. The conditional probability of the event $\mathcal{A}$ given that event $\mathcal{B}$ has happened is given by:

$$P(\mathcal{A}|\mathcal{B}) = \frac{P(\mathcal{A} \bigcap \mathcal{B})}{P(\mathcal{B})} \ , \tag{4.15}$$

where $P(\mathcal{A} \bigcap \mathcal{B})$ is the probability of both $\mathcal{A}$ and $\mathcal{B}$ happening. Similarly, we can write for the probability that $\mathcal{B}$ is true given that $\mathcal{A}$ is true:

$$P(\mathcal{B}|\mathcal{A}) = \frac{P(\mathcal{A} \bigcap \mathcal{B})}{P(\mathcal{A})} \ . \tag{4.16}$$

Eliminating $P(\mathcal{A} \bigcap \mathcal{B})$ from the above two equations, we get:

$$P(\mathcal{B}|\mathcal{A}) = \frac{P(\mathcal{B})P(\mathcal{A}|\mathcal{B})}{P(\mathcal{A})} \ . \tag{4.17}$$

Now since $P(\mathcal{A}) = P(\mathcal{B})P(\mathcal{A}|\mathcal{B}) + P(\neg\mathcal{B})P(\mathcal{A}|\neg\mathcal{B})$, we can write:

$$P(\mathcal{B}|\mathcal{A}) = \frac{P(\mathcal{B})P(\mathcal{A}|\mathcal{B})}{P(\mathcal{B})P(\mathcal{A}|\mathcal{B}) + P(\neg\mathcal{B})P(\mathcal{A}|\neg\mathcal{B})} = \frac{\Lambda(\mathcal{B}|\mathcal{A})}{\Lambda(\mathcal{B}|\mathcal{A}) + P(\neg\mathcal{B})/P(\mathcal{B})} \ , \tag{4.18}$$

where we define the likelihood ratio $\Lambda(\mathcal{B}|\mathcal{A})$ as:

$$\Lambda(\mathcal{B}|\mathcal{A}) = \frac{P(\mathcal{A}|\mathcal{B})}{P(\mathcal{A}|\neg\mathcal{B})} = \frac{p(\mathcal{A}|\mathcal{B})}{p(\mathcal{A}|\neg\mathcal{B})} \ , \tag{4.19}$$

where in the last step the probabilities have been replaced by respective probability densities.

### 4.1.3 Matched Filter

To distinguish between the two hypotheses mentioned above, we would like to compute the likelihood ratio for the alternate hypothesis. That is,

$$\Lambda(\mathcal{H}_1|s) = \frac{p(s|\mathcal{H}_1)}{p(s|\mathcal{H}_0)} \ . \tag{4.20}$$

We can now compute the probability densities, assuming the noise is Gaussian. We can assume the noise to be Gaussian since its coming from multiple sources as multiple independent components, which turns out more or less Gaussian. The probability distribution function for a Gaussian random process with mean $\mu$ and variance $\sigma^2$ is :

$$f(x|\mu,\sigma^2) = \frac{1}{\sigma\sqrt{2\pi}} e^{-\frac{(x-\mu)^2}{2\sigma^2}} \ . \tag{4.21}$$

For the alternate hypothesis,

$$p(s|\mathcal{H}_1) = p_n[s(t)] \propto e^{-(s,s)/2} \ , \tag{4.22}$$

while for the null hypothesis,

$$p(s|\mathcal{H}_0) = p_n[s(t) - h(t)] \propto e^{-(s-h,s-h)/2} \ , \tag{4.23}$$

so that the likelihood ratio becomes:

$$\Lambda(\mathcal{H}_1|s) = \frac{e^{-(s-h,s-h)/2}}{e^{-(s,s)/2}} = e^{(s,h)}\, e^{-(h,h)/2} \ . \tag{4.24}$$

This motivates us to define the inner product $(s,h)$ as the *matched filter*:

$$(s,h) = 4\, Re \int_{f_{low}}^{f_{up}} \frac{\tilde{s}(f)\tilde{h}^*(f)}{S_n(f)} df \ . \tag{4.25}$$

In Eq.(4.25), $f_{up}$ and $f_{low}$ are the lower and upper frequency cutoffs, respectively. We can choose the upper frequency cutoff to be that corresponding to the Innermost Stable Circular Orbit (ISCO), which means an orbital separation of $3R_s$, where $R_S$ is the Schwarzschild radius.

The matched filter is essentially the noise-weighted correlation of the strain data with an anticipated signal. We see that the likelihood ratio only depends on the data $s(t)$ through the matched filter. Also, the likelihood ratio is a monotonically increasing function of the matched filer. This gives us an ideal choice for the optimal detection statistic, since any threshold we set for the likelihood ratio for claiming that the alternative hypothesis is true can be computed using the matched filter. That is, if we set a threshold $k$ on the likelihood ratio, then if $\Lambda(\mathcal{H}_1|s) \geq k$ then we adopt the alternate hypothesis. And if $\Lambda(\mathcal{H}_1|s) \leq k$ then we adopt the null hypothesis. Setting a threshold also decides the false-alarm rate. A lower threshold value will give high false alarm rate.

### 4.1.4 Statistical Properties of the Matched Filter

Let a gravitational wave signal be $h(t;A)$ where $A$ is the (unknown) amplitude of the signal. If $h(t;A)$ has a known signal form $g(t)$, the logarithm of the likelihood ratio will be:

$$\ln \Lambda(\mathcal{H}|s) = (s, h(A)) - \frac{1}{2}(h(A), h(A)) = A(s,g) - \frac{1}{2}A^2(g,g) \ . \tag{4.26}$$

We get the amplitude $A_{max}$ when the above equation is maximized:

$$A_{max} = \frac{(s,g)}{(g,g)} \ . \tag{4.27}$$

Putting this back in the equation gives us the maximum log-likelihood ratio:

$$\ln \Lambda(\mathcal{H}|s) = \frac{1}{2}\frac{(s,g)^2}{(g,g)} \ . \tag{4.28}$$

We call the signal form $g(t)$ as a template. It is proportional to the anticipated signal.

Now, it can be easily shown when there is no signal, the variance of the matched filter (Eq. 4.25) is $\sigma^2 = (g,g)$. This is because we assume that the noise is zero mean Gaussian random process. When a signal $h(t;A)$ is present:

$$< x >=< (s,g) > +(h,g) = A\sigma^2 \ , \tag{4.29}$$

$$< x^2 >= \sigma^2 + A^2\sigma^4 \ , \tag{4.30}$$

so that the variance:

$$\mathrm{Var}(x) =< x^2 > - < x >^2 = \sigma^2 \ . \tag{4.31}$$

This means that the matched filter $x = (s,g)$ is a Gaussian random variable in the presence of a signal.

We can now define the signal-to-noise ratio (SNR) as $\rho = x/\sigma$. It is a normalized matched filter that is a Gaussian random variable. When there is no signal, it has zero mean and unit variance ($< \rho >= 0; \mathrm{Var}(\rho) = 1$). When a signal is present, the mean becomes equal to $(h,h)^{1/2}$.

## 4.2 Template Banks

Usually, $h(t)$ will be dependent on a set of parameters, say $\lambda_i$. For a gravitational wave signal this could be the masses, spins, etc. Let all these parameters be represented by a vector $\boldsymbol{\lambda} = [\lambda_1, ..., \lambda_N]$ in an $N$-dimensional parameter space. The signal can now be written as $h(t;\boldsymbol{\lambda})$.

We do not know *a priori* what should be chosen for the template $g(t;\boldsymbol{\lambda})$. The signal can be in any region of the parameter space. Thus, we have to discretize the parameter space sufficiently finely and compute the template at each of these points. Then, the maximum likelihood ratio can be identified as the template which has the best match. Each of these templates is normalized $(u(t;\boldsymbol{\lambda}), u(t;\boldsymbol{\lambda})) = 1$ so that the SNR $\rho(\lambda) = (s, u(t;\boldsymbol{\lambda}))$.

This set of templates, $u(t;\boldsymbol{\lambda})$, called as the template bank, has to constructed so that the signal $h(t;\boldsymbol{\lambda})$ should lie close enough to one of the templates. The fitting factor $\mathcal{F}$ tells us how well the template waveforms match a true signal:

$$\mathcal{F} =_{\boldsymbol{\lambda}}^{max} \frac{(h, u(\boldsymbol{\lambda}))}{\sqrt{(h,h)}} \ . \tag{4.32}$$

### 4.2.1 Placement of the Templates

In Sec.(4.1.4), it was described how we can maximize over extrinsic parameters such as the amplitude. The other extrinsic parameters can also be dealt with similarly. However, we need to search over the intrinsic parameters over which the GW signal would depend. For example, for CBCs, these could be the masses, spins, etc. So we have to place the templates in the template banks densely. Since it is computationally impossible to place the templates extremely densely, we compromise by reducing the number of templates - we allow the number of templates to minimize such that the maximum mismatch between the signal and the template does not go beyond a tolerable value. If we allow for 10% loss of the signals, it corresponds to 3% loss in SNR.

This mismatch can be quantified in terms of the ambiguity function, defined as:

$$\mathcal{A}(\boldsymbol{\lambda}, \boldsymbol{\lambda}') = (u(\boldsymbol{\lambda}), u(\boldsymbol{\lambda}')) \ , \tag{4.33}$$

where the templates $u(\boldsymbol{\lambda})$ are normalized. That means, they lie on a submanifold of a hyperspace of $N-1$ dimensions.

Now, expand $\boldsymbol{\lambda}' = \boldsymbol{\lambda} + \Delta\boldsymbol{\lambda}$ with small $\Delta\boldsymbol{\lambda}$ so that we only allow for 3% mismatch. The ambiguity function, then, becomes:

$$\mathcal{A}(\boldsymbol{\lambda}, \boldsymbol{\lambda} + \Delta\boldsymbol{\lambda}) \simeq 1 + \frac{1}{2}\frac{\partial^2 \mathcal{A}}{\partial\boldsymbol{\lambda}^\alpha \partial\boldsymbol{\lambda}^\beta}\Delta\boldsymbol{\lambda}^\alpha \Delta\boldsymbol{\lambda}^\beta \ , \tag{4.34}$$

where the metric $g_{\alpha\beta}$ has been used:

$$g_{\alpha\beta} = -\frac{1}{2}\frac{\partial^2 \mathcal{A}}{\partial\boldsymbol{\lambda}^\alpha \partial\boldsymbol{\lambda}^\beta} \ , \tag{4.35}$$

If we had defined the maximum mismatch to be $\in$ then $\mathcal{A}((\lambda),(\lambda)') \geq 1- \in=$ minimum match. So, if we allow for 3% loss in SNR, then $\in= 0.03$ and minimum match $= 0.97$. The placement of the templates is then described as:

$$g_{\alpha\beta}\Delta\boldsymbol{\lambda}^{\alpha}\Delta\boldsymbol{\lambda}^{\beta} =\in , \tag{4.36}$$

## 4.3 Detection of Gravitational Waves from Compact Binaries

The technique of matched filtering works very well for CBCs since we can model the GW signal coming from such sources, as was discussed in Sec. 2.3.1 and Sec. 2.3.2. We create a template bank of waveforms which spans the relevant parameter space. Instead of NR waveforms, we use the various approximants to generate the waveforms for the template bank, because NR waveforms take too much computational resources and time. Template banks may contain $\sim 1$ million points in the parameter space and it is not feasible to generate NR waveforms for each of these points.

We can generate waveforms, place the template banks, calculate match, etc. using LALSUITE [22](a package developed by the LSC) and/or PyCBC [37](a python toolkit for data analysis of GWs from CBCs). Using these tools, we can check if a given GW signal is detectable using a certain template bank. We can also determine the parameters that the signal is characterized by.

We can create waveforms from the approximants and treat them as GW signals. These are called as "injections". Also, as mentioned before, we can create template banks using the available approximants and then check if the template banks can recover the injections from the noisy data using matched filtering. This is done by calculating the fitting factors, which tell us how effectual the approximant we used for template bank is for detection of GW signal.

The purpose of this project is to test the effectualness of approximants SEOBNRv2-ROM-DoubleSpin, IMRPhenomD and TaylorF2RedSpin using current pipelines available in LALSUITE/PyCBC in recovering GW signals from SOR binaries.

# Chapter 5

# Results and Conclusion

For the purpose of this project, we model SOR GW signals by using two kinds of waveform approximants: SpinTaylorT4 and SEOBNRv3 (see Sec. 2.3.2 for more details). SpinTaylorT4 models only the inspiral phase of the waveform, while SEOBNRv3 models the entire Inspiral-Merger-Ringdown waveform. For generating the template bank to recover these signals, we use three approximants: TaylorF2RedSpin, IMRPhenomD and SEOBNRv2-ROM-DoubleSpin. TaylorF2RedSpin is an inspiral-only waveform, while IMRPhenomD and SEOBNRv2 are full IMR waveforms. All the three template approximants are aligned-spin, i.e. their spins are aligned with the orbital angular momentum, while the spins of the injected signals follow the SOR condition and may not be aligned to the orbital angular momentum. We also have injections for generic precessing binaries, for which the spins may oriented in any possible way. This chapter begins with giving the details of the parameters used for SOR signals and template banks in the study.

## 5.1 Parameters Used

The various parameters used for the simulations are as follows:

- **INJECTIONS**
  - **Waveform Approximant**: SpinTaylorT4 and SEOBNRv3 (SOR $\Delta\phi =$ 0°, SOR $\Delta\phi =$180° and generic)
  - **Mass ratio ($q$) range**: 1 - 3
  - **Total Mass ($m$) range**: $6M_\odot - 20M_\odot$ for SpinTaylorT4 and $6M_\odot - 64M_\odot$ for SEOBNRv3
  - **Spin magnitude ($\chi_1, \chi_2$) range**: 0.5 - 0.98
  - **Lower cutoff (f-low) frequency**: 20Hz
  - **Number of injections**: 10,000

- **TEMPLATE BANKS**
  - **Waveform Approximant**: TaylorF2RedSpin, SEOBNRv2-ROM-DoubleSpin, IMRPhenomD
  - **Noise PSD**: aLIGOZeroDetHighPower
  - **Minimum Match** $(1- \in)$: 0.97
  - **Lower cutoff (flow) frequency**: 20Hz
  - **Component Mass** $(m_1, m_2)$ **range**: $3M_\odot - 30M_\odot$ for SpintaylorT4 Injections and $3M_\odot - 50M_\odot$ for SEOBNRv3 injections
  - $z$**-component spin range**: $-0.99, 0.99$

The simulations involve computing the fitting factor values for the various kinds of injections. We can compare the various template approximants on the basis of the fitting factor values we obtain. The results are shown by plotting cumulative histogram of the fitting factor values for all the 10000 injections. The following section contains the results obtained for injections modelled by SpinTaylorT4, while the section after that shows the results of SEOBNRv3 injections.

## 5.2 SpinTaylorT4 Injections

### 5.2.1 Effect of Truncating the Waveform at Innermost Stable Circular Orbit

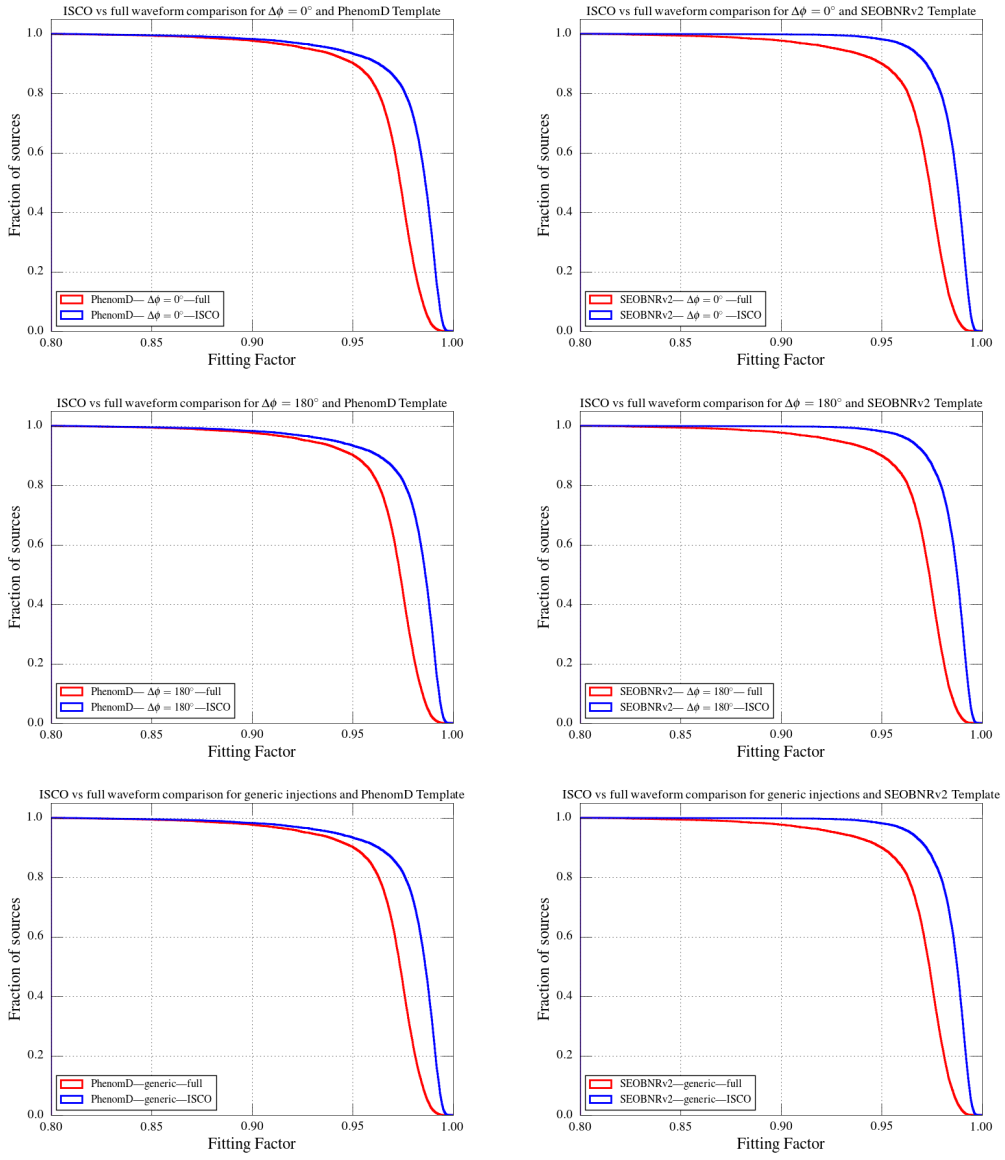


Figure 5.1: We plot the cumulative histogram of the fitting factors against the fraction of sources. The left panel is for IMRPhenomD template, while the right panel is for SEOBNRv2-ROM-DoubleSpin template. The top panel describes $\Delta\phi = 0°$ family, the middle $\Delta\phi = 180°$ family, and the bottommost generic binaries.

Since our injections are inspiral-only waveform, we investigate the effects of truncating the template waveforms at ISCO. We can clearly see that terminating the waveform at frequency corresponding to ISCO improves the performance in all the cases of SEOBNRv2 and IMRPhenomD templates. We do not study for TaylorF2RedSpin as it is already inspiral-only waveform.

### 5.2.2 Comparison of Performance of Template Banks

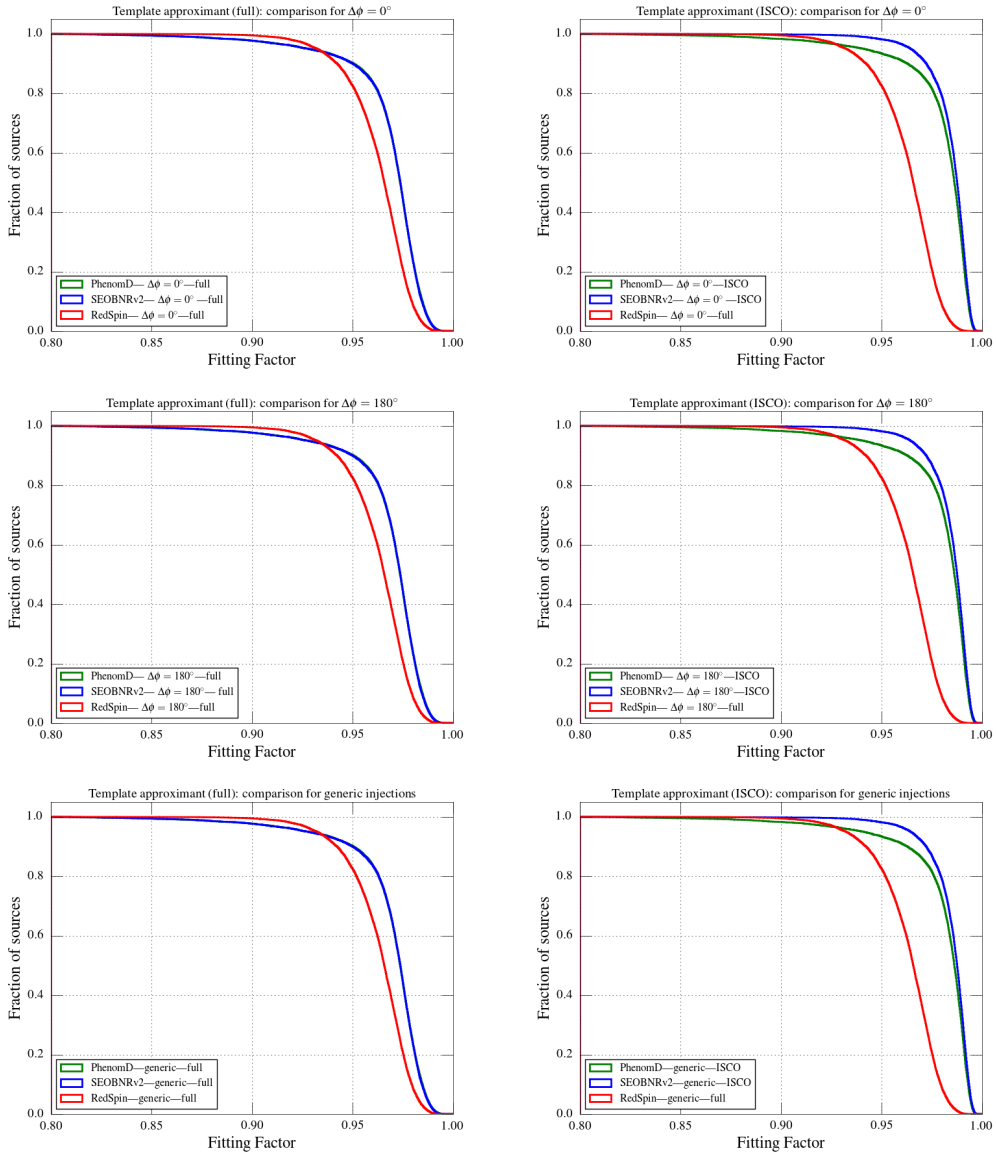


Figure 5.2: We plot the cumulative histogram of the fitting factors against the fraction of sources. The left panel is for full IMR waveforms for IMRPhenomD and SEOBNRv2, while in the right panel these are truncated at ISCO. The top panel describes $\Delta\phi = 0°$ family, the middle $\Delta\phi = 180°$ family, and the bottommost generic binaries.

In the Fig. 5.2 we compare the performance of the three approximants used to create the template banks, namely IMRPhenomD, SEOBNRv2-ROM-DoubleSpin and TaylorF2RedSpin. We see that if we take the full IMR waveform to generate the template bank, IMRPhenomD and SEOBNRv2 behave almost similarly, at the same time yielding higher fitting factors than TaylorF2RedSpin. Hence, these approximants perform better than TaylorF2RedSpin. If we terminate the waveform at ISCO, the performance improves even further, with SEOBNRv2 recovering the SOR signal better than IMRPhenomD.

### 5.2.3 Comparison between recovery of Spin Orbit Resonances and Generic Binaries

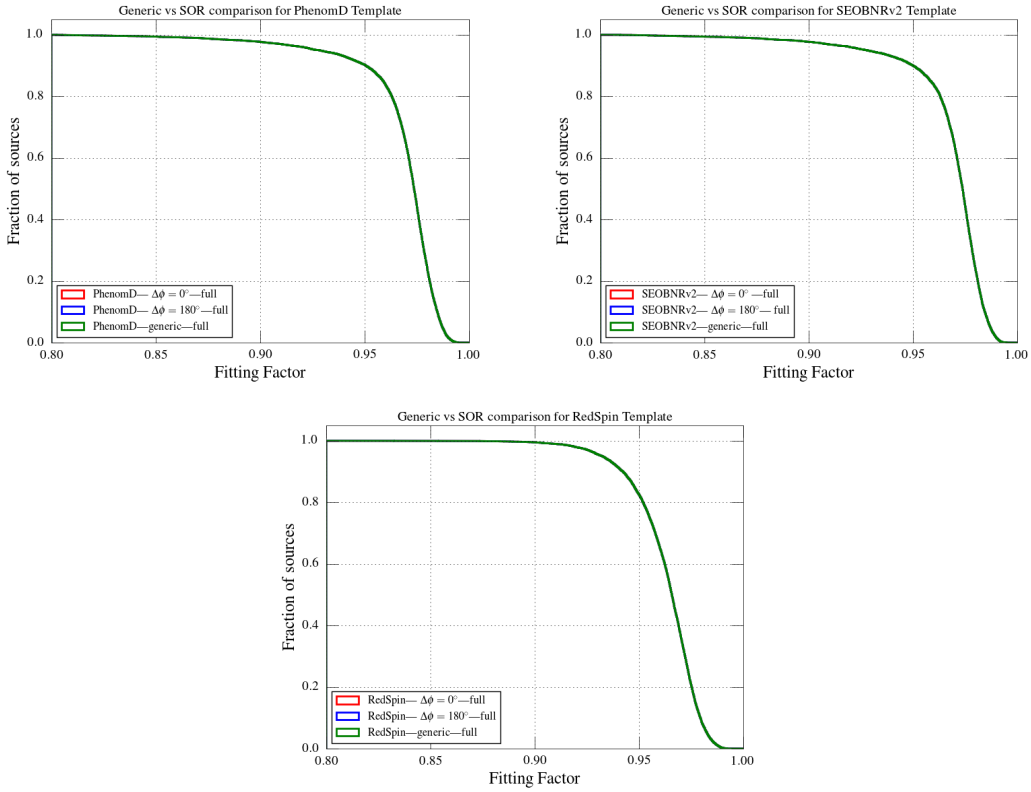


Figure 5.3: We plot the cumulative histogram of the fitting factors against the fraction of sources. The first figure is for IMRPhenomD template, the second for SEOBNRv2 template and the third for TaylorF2RedSpin template.

Here, we want to compare the performance of a template approximant over the three kinds of injections - SOR binary belonging to $\Delta\phi = 0°$ family, SOR binary belonging to $\Delta\phi = 180°$ family and generic precessing binaries with high spins. Since SOR binaries have fewer degrees of freedom than the generic precessing binaries, we expect that the fitting factors for them would be more than, or at least equal to, those of generic precessing sources. We find that the recovery for all the types of injections is remarkably similar. This is also true no matter what template approximate we choose.

### 5.2.4 High Spin vs Low Spin: Comparison

#### IMRPhenomD

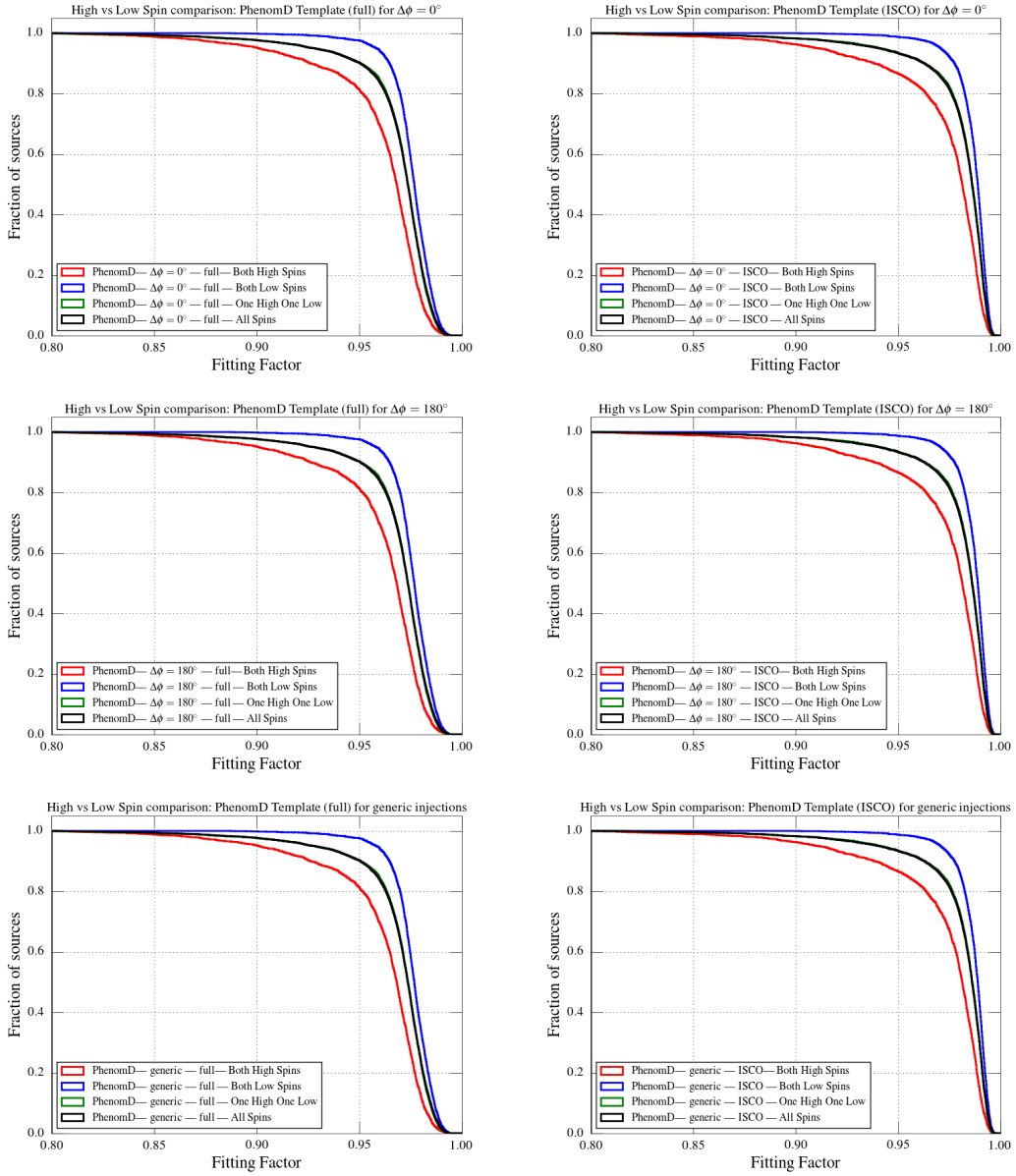


Figure 5.4: We plot the cumulative histogram of the fitting factors against the fraction of sources recovered by IMPRPhenomD. The left panel is for full IMR waveforms, while in the right panel these are truncated at ISCO. The top panel describes $\Delta\phi = 0°$ family, the middle $\Delta\phi = 180°$ family, and the bottommost generic binaries.

## SEOBNRv2

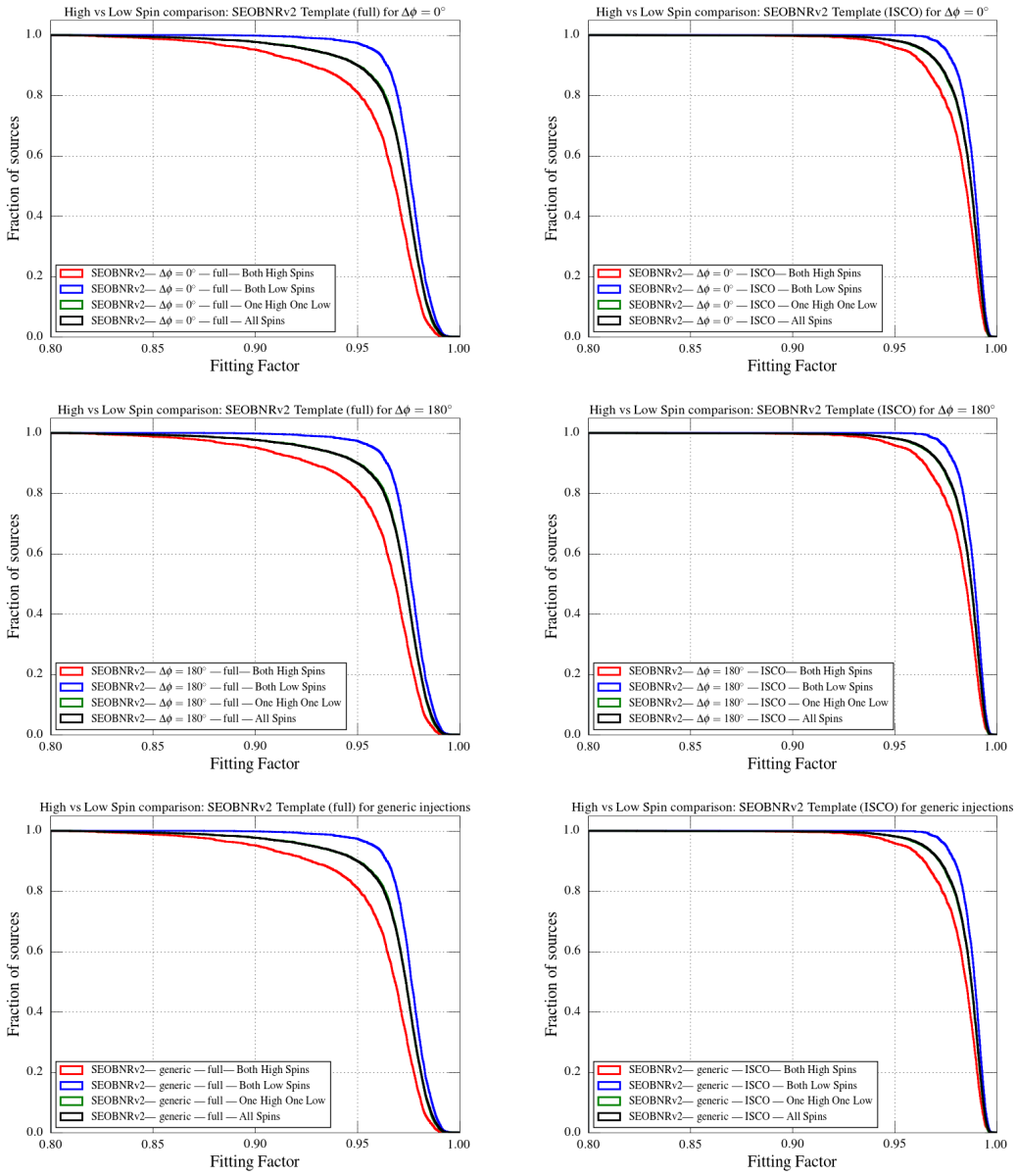


Figure 5.5: We plot the cumulative histogram of the fitting factors against the fraction of sources recovered by SEOBNRv2-ROM-DoubleSpin. The left panel is for full IMR waveforms, while in the right panel these are truncated at ISCO. The top panel describes $\Delta\phi = 0°$ family, the middle $\Delta\phi = 180°$ family, and the bottommost generic binaries.

### TaylorF2RedSpin

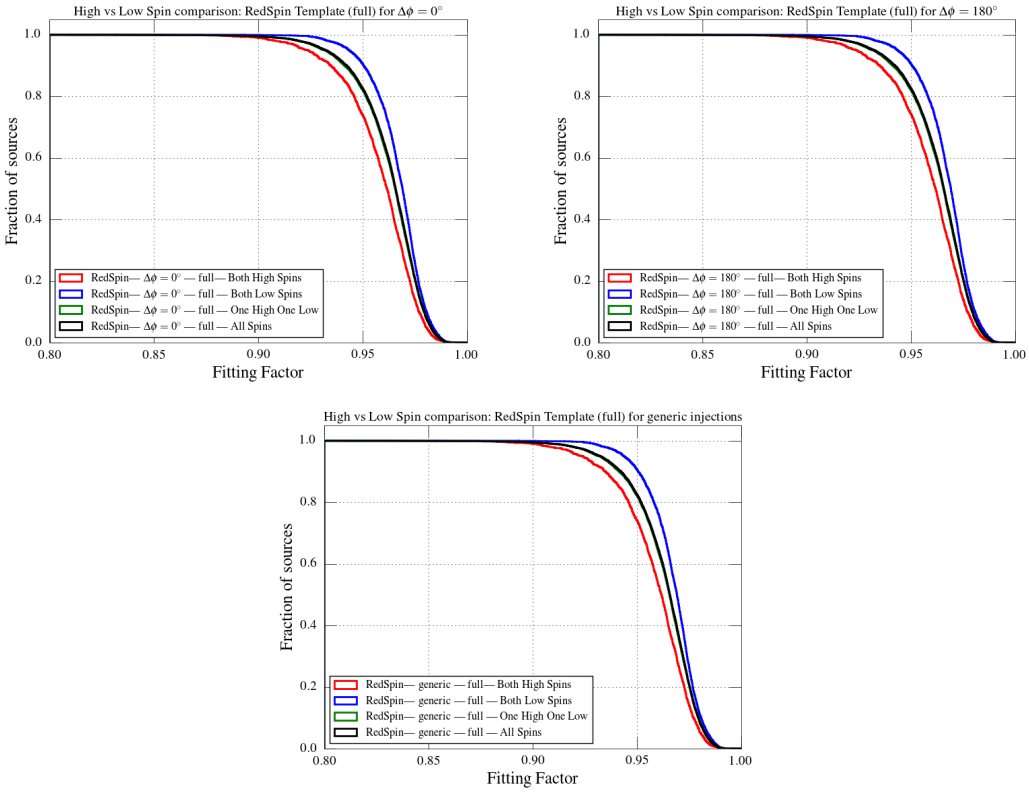


Figure 5.6: We plot the cumulative histogram of the fitting factors against the fraction of sources recovered by TaylorF2RedSpin. The first plot describes $\Delta\phi = 0°$ family, the second $\Delta\phi = 180°$ family, and the bottommost generic binaries.

We know that different approximants use different effective spins as one of their free parameters. Here we study how effectual these approximants are for different regions in the spin parameter space. Our injections have their spins lying between $0.5 - 0.98$. We further divide them into three categories: high spins - if spins of both the component masses are above 0.75, low spins - if spins of both the component masses are in the range 0.5 -0.75, and the third category includes the injections for which the spin of only one component mass is above 0.75 and that of other is below 0.75.

From the results of comparison, we can see that low spin injections are recovered better than high spins for all template banks and all injection configurations. The injections with one high and one low spin have similar fitting factors to the case when we are considering all the spins at once.

**Comparison of Performance of Template Banks for High Spin and low spin Signals: full IMR template waveforms**

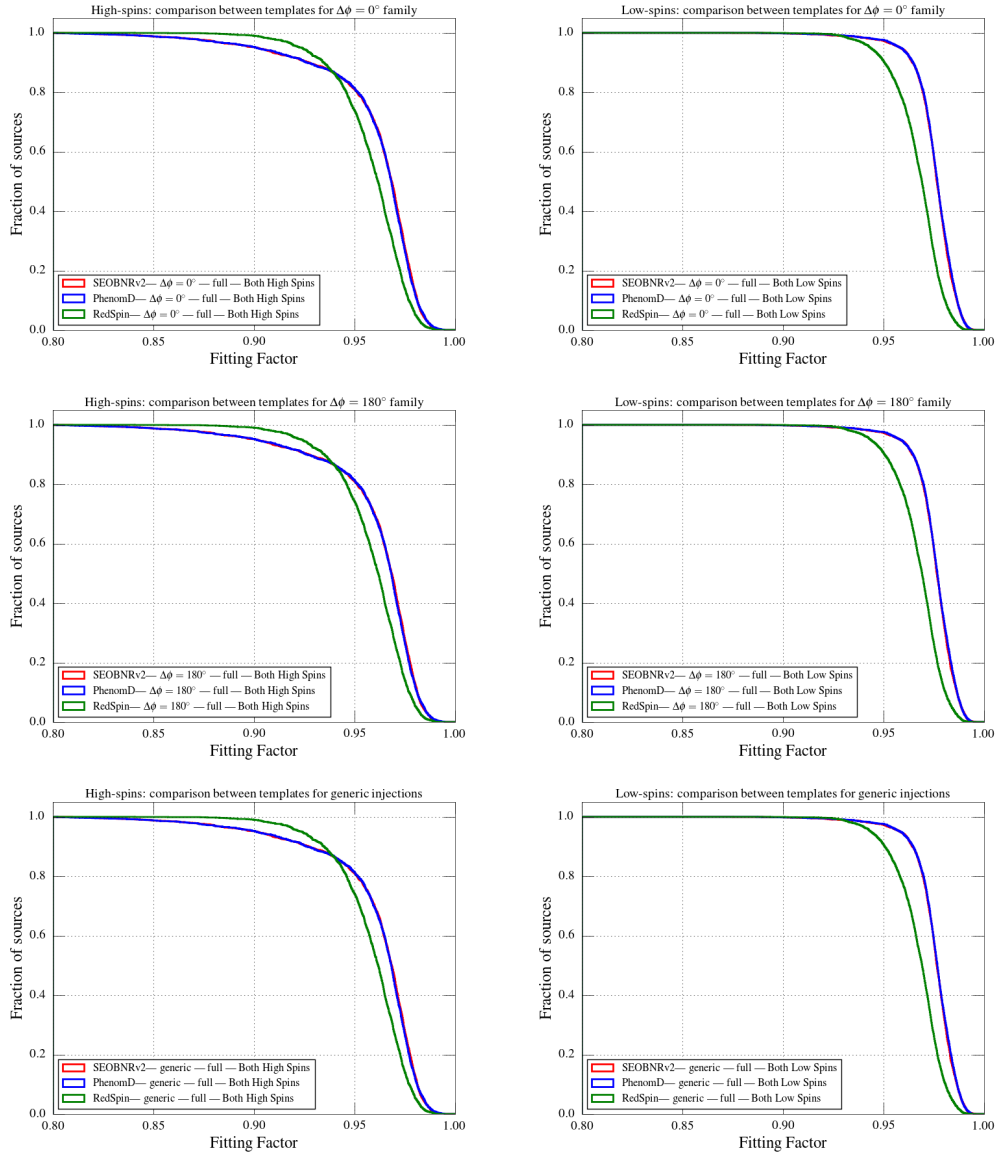


Figure 5.7: We plot the cumulative histogram of the fitting factors against the fraction of sources for high spins (left panel) and low spins (right panel) separately for all three template approximants using their entire waveform. The top panel describes $\Delta\phi = 0^\circ$ family, the middle $\Delta\phi = 180^\circ$ family, and the bottommost generic binaries.

**Comparison of Performance of Template Banks for High spin and Low spin signals: IMR templates trunctaed at ISCO**

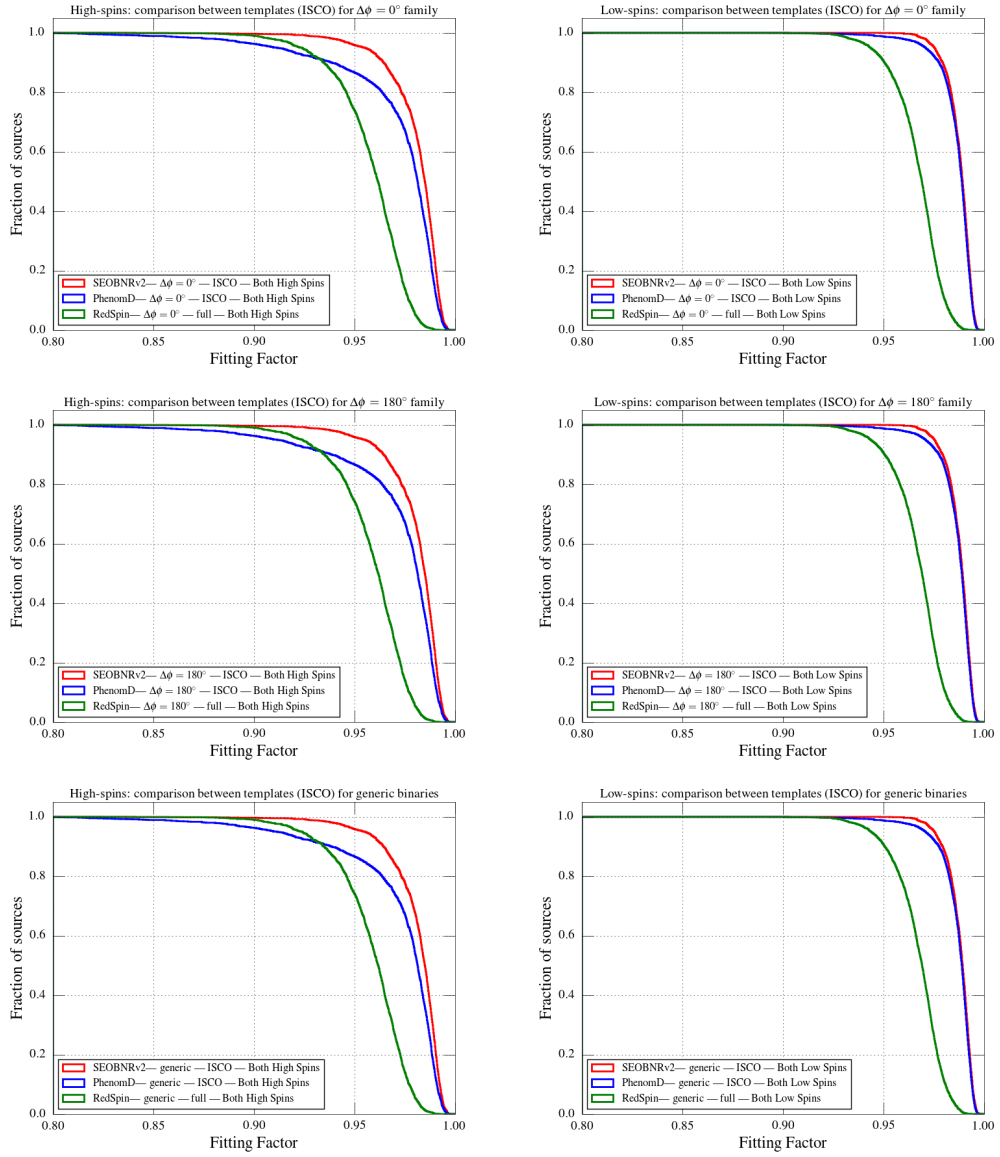


Figure 5.8: We plot the cumulative histogram of the fitting factors against the fraction of sources for high spins (left panel) and low spins (right panel) separately for all three template approximants with their waveforms terminated at ISCO. The top panel describes $\Delta\phi = 0°$ family, the middle $\Delta\phi = 180°$ family, and the bottommost generic binaries.

## 5.3 SEOBNRv3 Injections

### 5.3.1 Comparison of Performance of Template Banks

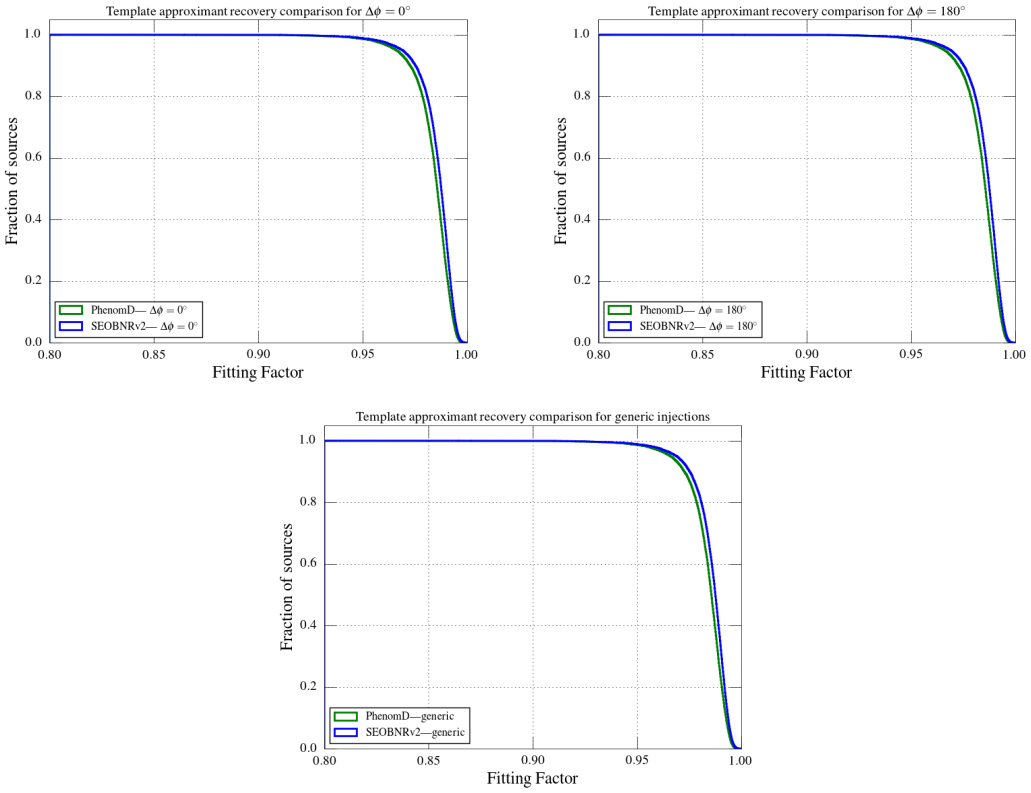


Figure 5.9: We plot the cumulative histogram of the fitting factors against the fraction of sources. The first plot describes $\Delta\phi = 0°$ family, the second $\Delta\phi = 180°$ family, and the bottommost generic binaries.

In the Fig. 5.9 we compare the performance of the two approximants used to create the template banks, namely IMRPhenomD and SEOBNRv2-ROM-DoubleSpin. We see that the recovery of the injections by SEOBNRv2 is marginally more than IMRPhenomD.

### 5.3.2 Comparison between recovery of Spin Orbit Resonances and Generic Binaries

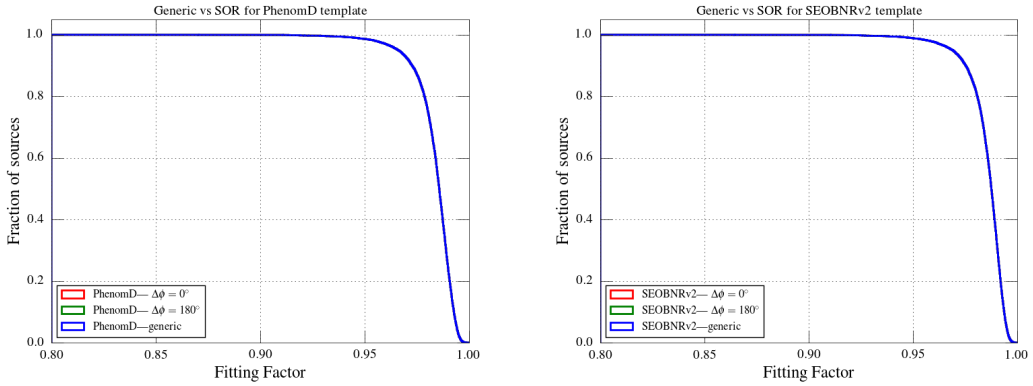


Figure 5.10: We plot the cumulative histogram of the fitting factors against the fraction of sources. The first figure is for IMRPhenomD template and the second for SEOBNRv2 template.

Here, we want to compare the performance of a template approximant over the three kinds of injections - SOR binary belonging to $\Delta\phi = 0°$ family, SOR binary belonging to $\Delta\phi = 180°$ family and generic precessing binaries with high spins. The results for this study with SEOBNRv3 injections is the same as that for SpinTaylorT4 - the recovery of all the types of injections is almost the same, no matter what template approximant we use.

## 5.4 Discussion and Conclusion

In this thesis, we test the performance of various template banks employed in the detection pipelines used in the CBC searches in detecting GWs from the Spin Orbit Resonant (SOR) binaries. The template approximants used to model these banks are :

- **SEOBNRv2-ROM-DoubleSpin**: This has the entire IMR waveform, has its spins aligned to the orbital angular momentum , and uses the Effective-One-Body approximation to generate the waveform.
- **IMRPhenomD**: This has the entire IMR waveform, is aligned spin, and is the lates phenomenological waveform model.

- **TaylorF2RedSpin** : This is inspiral-only waveform, is aligned-spin, and uses an effective spin to model the waveform.

We also had two different approximants used to model the GW signal which are used as injections:

- **SpinTaylorT4** : This is an inspiral only approximant. However, the spins can be oriented in any direction with respect to the orbital angular momentum.

- **SEOBNRv3** : This approximant generates the entire IMR waveform and spins may not be aligned to the orbital angular momentum. This approximant uses the Effective-One-Body approximation to generate the waveform.

We find that SEOBNRv2 and PhenomD perform better than RedSpin templates. The performance in recovering injections from SOR binaries is the same as that for generic precessing binaries. Additionally, we have also presented Schnittman's equilibrium configurations for sub-maximally spinning BBHs.

For SpinTaylorT4 injections, we tested the effectualness of SEOBNRv2 and IMRPhenomD in recovering generic and SOR injections by providing a high-frequency cutoff at the Innermost Stable Circular Orbit (ISCO). We found that their performance improves after doing so, as compared to the case when their entire IMR waveform is being used. It is because the injections have inspiral part only, and recovering them through IMR template waveforms would result in higher mismatch.

Using SpinTaylorT4 as injection approximant, if we make a comparison between the performance of the template approximants, we find that TaylorF2RedSpin can only recover $\sim 80\%$ of the sources with fitting factors higher than 0.95. SEOBNRv2 and IMRPhenomD, using their full IMR waveform, can yield $\sim 90\%$ of injections with fitting factors higher than 0.95. However, if we cutoff their waveforms at ISCO, the recovery fraction of injections with fitting factors higher than 0.95 goes to $\sim 93\%$ for IMRPhenomD and as high as $\sim 98\%$ for SEOBNRv2.

When we use SEOBNRv3 as the waveform approximant for modelleing GW signals as injections, we see that SEOBNRv2 performs marginally better than IMRPhenomD. Both recover $\sim 98\%$ of sources with fitting factor values higher than 0.95.

We also show that the magnitude of the spins play an important role in determining the fitting factors. The general trend that was observed was that injections with low spins (spins of both components lower than 0.75) are recovered better than the injections with high spins. For all the three approximants, low spin had $\sim 20\%$ more sources that had fitting factors more than 0.95 as compared to high spins, when using their full IMR waveform. If the waveform is cutoff at ISCO, $\sim 98\%$ of the sources with low spins have fitting factor more than 0.95 for IMRPhenomD, while 100% of the low spinning injections had fitting factor more than 0.96 for SEOBNRv2.

We also compared the performance of different templates banks for different regions in the spin parameter space. For low spin cases, considering full IMR waveforms, we found that SEOBNRv2-ROM-DoubleSpin and IMRPhenomD perform equally well, but better as compared to TaylorF2RedSpin. For high spin cases, both these waveforms recover $\sim 80\%$ injections while TaylorF2RedSpin recovers $\sim 70\%$.

When we truncate the IMR waveforms at ISCO, SEOBNRv2 performs the best in recovering injections in both the cases. The performance of IMRPhenomD is also better than TaylorF2RedSpin, and it improves in recovering low spin injections as compared to recovering high spin injections.

The main motive of the project was to test the effectualness of the approximants - SEOBNRv2-ROM-DoubleSpin, IMRPhenomD and TaylorF2RedSpin - in recovering SOR signals (from both families $\Delta\phi = 0^\circ$ and $\Delta\phi = 180^\circ$). We find that $\sim$ 90% of the sources had their fitting factors higher than 0.95 when SEOBNRv2 or IMRPhenomD were used to create template waveforms. The fraction decreased to $\sim$80% in the case of TaylorF2RedSpin templates.

Also, SOR binaries have two degrees of freedom less than the general precessing binary system. Hence it was expected that the fitting factors obtained for SOR binaries would be not less than those of generic precessing binaries. It is found that the generic precessing binaries and SOR binaries are recovered equally well.

It will be interesting to do similar studies with NR waveforms computed for SOR binaries. These NR waveforms are believed to be the most accurate ones and will give us more insight about the detectability of such systems. One can further perform Parameter Estimation studies for the same approximants. The future work may also include generating template banks following the SOR conditions.

# References


[1] B. P. Abbott, R. Abbott, T. D. Abbott, M. R. Abernathy, F. Acernese, K. Ackley, C. Adams, T. Adams, P. Addesso, R. X. Adhikari, et al., Observation of Gravitational Waves from a Binary Black Hole Merger, Physical Review Letters 116 (6) (2016) 061102. arXiv:1602.03837, doi:10.1103/PhysRevLett.116.061102.

[2] R. Hulse, J. Taylor, Discovery of a pulsar in a binary system, Neutron stars, black holes, and binary X-ray sources 48 (1975) 433.

[3] J. D. Creighton, W. G. Anderson, Gravitational-Wave Physics and Astronomy: An Introduction to Theory, Experiment and Data Analysis, John Wiley & Sons, 2012.

[4] M. Maggiore, Gravitational waves. vol 1, theory and experiments.

[5] [link].
URL http://www.gravity.uwa.edu.au/photo/stageone/Fig3.jpg

[6] B. S. Sathyaprakash, B. F. Schutz, Physics, Astrophysics and Cosmology with Gravitational Waves, Living Reviews in Relativity 12. arXiv:0903.0338, doi:10.12942/lrr-2009-2.

[7] T. Damour, B. R. Iyer, B. S. Sathyaprakash, Improved filters for gravitational waves from inspiraling compact binaries, Phys. Rev. D 57 (1998) 885–907. doi:10.1103/PhysRevD.57.885.
URL http://link.aps.org/doi/10.1103/PhysRevD.57.885

[8] J. Abadie, B. P. Abbott, R. Abbott, M. Abernathy, T. Accadia, F. Acernese, C. Adams, R. Adhikari, P. Ajith, B. Allen, et al., TOPICAL REVIEW: Predictions for the rates of compact binary coalescences observable by ground-based gravitational-wave detectors, Classical and Quantum Gravity 27 (17) (2010) 173001. arXiv:1003.2480, doi:10.1088/0264-9381/27/17/173001.

[9] J. Aasi, et al., Prospects for Observing and Localizing Gravitational-Wave Transients with Advanced LIGO and Advanced Virgo[Living Rev. Rel.19,1(2016)]. arXiv:1304.0670, doi:10.1007/lrr-2016-1.

[10] F. Mannucci, M. Della Valle, N. Panagia, How many supernovae are we missing at high redshift?, Monthly Notices of the Royal Astronomical Society 377 (2007) 1229–1235. arXiv:astro-ph/0702355, doi:10.1111/j.1365-2966.2007.11676.x.

[11] J. Aasi, J. Abadie, B. P. Abbott, R. Abbott, M. Abernathy, T. Accadia, F. Acernese, C. Adams, R. Adhikari, P. Ajith, B. Allen, et al., Directed search for continuous gravitational waves from the galactic center, Phys. Rev. D 88 (2013) 102002. doi:10.1103/PhysRevD.88.102002.
URL http://link.aps.org/doi/10.1103/PhysRevD.88.102002

[12] A. Buonanno, M. Maggiore, C. Ungarelli, Spectrum of relic gravitational waves in string cosmology, Phys. Rev. D 55 (1997) 3330–3336. doi:10.1103/PhysRevD.55.3330.
URL http://link.aps.org/doi/10.1103/PhysRevD.55.3330

[13] A. A. Starobinsky, JETP Lett. 30 682.

[14] [link].
URL https://www.ligo.caltech.edu/system/pages/images/27/page/basic_ifo_diagram.jpg?1432340449

[15] The LIGO Scientific Collaboration, the Virgo Collaboration, Tests of general relativity with GW150914, ArXiv e-printsarXiv:1602.03841.

[16] L. Blanchet, Gravitational Radiation from Post-Newtonian Sources and Inspiralling Compact Binaries, Living Reviews in Relativity 17. arXiv:1310.1528, doi:10.12942/lrr-2014-2.

[17] S. Chandrasekhar, The mathematical theory of black holes, 1983.

[18] L. Blanchet, B. R. Iyer, B. Joguet, Gravitational waves from inspiraling compact binaries: Energy flux to third post-newtonian order, Phys. Rev. D 65 (2002) 064005. doi:10.1103/PhysRevD.65.064005.
URL http://link.aps.org/doi/10.1103/PhysRevD.65.064005

[19] L. Blanchet, T. Damour, G. Esposito-Farèse, B. R. Iyer, Gravitational radiation from inspiralling compact binaries completed at the third post-newtonian order, Phys. Rev. Lett. 93 (2004) 091101. doi:10.1103/PhysRevLett.93.091101.
URL http://link.aps.org/doi/10.1103/PhysRevLett.93.091101

[20] L. Blanchet, G. Faye, B. R. Iyer, S. Sinha, The third post-newtonian gravitational wave polarizations and associated spherical harmonic modes for inspiralling compact binaries in quasi-circular orbits, Classical and Quantum Gravity 25 (16) (2008) 165003.
URL http://stacks.iop.org/0264-9381/25/i=16/a=165003

[21] [link].
URL http://www.black-holes.org/SpEC.html

[22] [link].
URL https://www.lsc-group.phys.uwm.edu/daswg/projects/lalsuite.html

[23] A. Buonanno, Y. Chen, M. Vallisneri, Detecting gravitational waves from precessing binaries of spinning compact objects: Adiabatic limit, Phys. Rev. D 67 (2003) 104025. doi:10.1103/PhysRevD.67.104025.
URL http://link.aps.org/doi/10.1103/PhysRevD.67.104025

[24] P. Ajith, Addressing the spin question in gravitational-wave searches: Waveform templates for inspiralling compact binaries with nonprecessing spins, Physical Review D 84 (8) (2011) 084037. arXiv:1107.1267, doi:10.1103/PhysRevD.84.084037.

[25] L. Santamaría, F. Ohme, P. Ajith, B. Brügmann, N. Dorband, M. Hannam, S. Husa, P. Mösta, D. Pollney, C. Reisswig, E. L. Robinson, J. Seiler, B. Krishnan, Matching post-newtonian and numerical relativity waveforms: Systematic errors and a new phenomenological model for nonprecessing black hole binaries, Phys. Rev. D 82 (2010) 064016. doi:10.1103/PhysRevD.82.064016.
URL http://link.aps.org/doi/10.1103/PhysRevD.82.064016

[26] A. Taracchini, A. Buonanno, Y. Pan, T. Hinderer, M. Boyle, D. A. Hemberger, L. E. Kidder, G. Lovelace, A. H. Mroué, H. P. Pfeiffer, M. A. Scheel, B. Szilágyi, N. W. Taylor, A. Zenginoglu, Effective-one-body model for black-hole binaries with generic mass ratios and spins, Phys. Rev. D 89 (2014) 061502. doi:10.1103/PhysRevD.89.061502.
URL http://link.aps.org/doi/10.1103/PhysRevD.89.061502

[27] A. Taracchini, Y. Pan, A. Buonanno, E. Barausse, M. Boyle, T. Chu, G. Lovelace, H. P. Pfeiffer, M. A. Scheel, Prototype effective-one-body model for nonprecessing spinning inspiral-merger-ringdown waveforms, Phys. Rev. D 86 (2012) 024011. doi:10.1103/PhysRevD.86.024011.
URL http://link.aps.org/doi/10.1103/PhysRevD.86.024011

[28] Y. Pan, A. Buonanno, A. Taracchini, L. E. Kidder, A. H. Mroué, H. P. Pfeiffer, M. A. Scheel, B. Szilágyi, Inspiral-merger-ringdown waveforms of spinning, precessing black-hole binaries in the effective-one-body formalism, Phys. Rev. D 89 (2014) 084006. doi:10.1103/PhysRevD.89.084006.
URL http://link.aps.org/doi/10.1103/PhysRevD.89.084006

[29] A. Buonanno, Y. Chen, M. Vallisneri, Detecting gravitational waves from precessing binaries of spinning compact objects: Adiabatic limit, Phys. Rev. D 67 (2003) 104025. doi:10.1103/PhysRevD.67.104025.
URL http://link.aps.org/doi/10.1103/PhysRevD.67.104025

[30] A. Gupta, A. Gopakumar, Probing evolution of binaries influenced by the spin-orbit resonances, Classical and Quantum Gravity 31 (10) (2014) 105017. arXiv:1312.0217, doi:10.1088/0264-9381/31/10/105017.

[31] T. A. Apostolatos, C. Cutler, G. J. Sussman, K. S. Thorne, Spin-induced orbital precession and its modulation of the gravitational waveforms from merging binaries, Phys. Rev. D 49 (1994) 6274–6297. doi:10.1103/PhysRevD.49.6274.
URL http://link.aps.org/doi/10.1103/PhysRevD.49.6274

[32] L. E. Kidder, Coalescing binary systems of compact objects to (post)$^{5/2}$-newtonian order. v. spin effects, Phys. Rev. D 52 (1995) 821–847. doi:10.1103/PhysRevD.52.821.
URL http://link.aps.org/doi/10.1103/PhysRevD.52.821

[33] J. D. Schnittman, Spin-orbit resonance and the evolution of compact binary systems, Physical Review D 70 (12) (2004) 124020. arXiv:astro-ph/0409174, doi:10.1103/PhysRevD.70.124020.

[34] M. Kesden, U. Sperhake, E. Berti, Relativistic Suppression of Black Hole Recoils, The Astrophysical Journal 715 (2010) 1006–1011. arXiv:1003.4993, doi:10.1088/0004-637X/715/2/1006.

[35] E. Berti, M. Kesden, U. Sperhake, Effects of post-Newtonian spin alignment on the distribution of black-hole recoils, Physical Review D 85 (12) (2012) 124049. arXiv:1203.2920, doi:10.1103/PhysRevD.85.124049.

[36] D. Gerosa, M. Kesden, E. Berti, R. O'Shaughnessy, U. Sperhake, Resonant-plane locking and spin alignment in stellar-mass black-hole binaries: A diagnostic of compact-binary formation, Physical Review D 87 (10) (2013) 104028. arXiv:1302.4442, doi:10.1103/PhysRevD.87.104028.

[37] [link].
URL http://ligo-cbc.github.io/pycbc/latest/html/